Article:
Senel, P., Lesnic, D. orcid.org/0000-0003-3025-2770 and Karageorghis, A. (Accepted: 2025) Meshless methods for the detection of an obstacle submerged in a two–dimensional Stokes flow. Engineering Analysis with Boundary Elements. ISSN: 0955-7997 (In Press)

Meshless methods for the detection of an obstacle submerged in a two–dimensional Stokes flow

Pelin Senel[1], **Daniel Lesnic**[2] and **Andreas Karageorghis**[3]

[1] Department of Mathematics, Karadeniz Technical University, 61080, Trabzon, Türkiye & Department of Applied Mathematics, University of Leeds, LS2 9JT, Leeds, United Kingdom
E-mail address: psenel@ktu.edu.tr

[2] Department of Applied Mathematics, University of Leeds, LS2 9JT, Leeds, United Kingdom
E-mail address: D.Lesnic@leeds.ac.uk

[3] Department of Mathematics and Statistics, University of Cyprus/Πανεπιστήμιο Κύπρου, P.O. Box 20537, 1678 Nicosia/Λευκωσία, Cyprus/Κύπρος
E-mail address: andreask@ucy.ac.cy

Abstract

We consider a geometric inverse problem which requires detecting an unknown obstacle, e.g. a submarine or an aquatic mine, submerged in a Stokes slow viscous stationary flow of an incompressible fluid. In two–dimensions, the problem is formulated in terms of the biharmonic streamfunction in an unbounded domain which is approximated using the Trefftz method and the method of fundamental solutions (MFS). This is, apparently, the first time the Trefftz method and the MFS are applied for the solution of the biharmonic equation in an unbounded domain. We first examine direct problems and then consider inverse problems. The unknown obstacle is determined by employing a nonlinear Tikhonov regularization procedure. Numerical results are presented and discussed.

Keywords: Biharmonic equation, Inverse geometric problem, Regularization, Stokes flow, Method of fundamental solutions, Trefftz method.

2010 AMS Subject Classification Codes: 49K20, 65N21, 65N80

1 Introduction

Inverse problems concerned with detecting an unknown obstacle concealed in a known host domain arise in a wide range of tomography screening applications in, e.g., medicine (tumour detection), security (landmine detection), geophysics (fault detection), amongst others. Inverse obstacle problems [20] are therefore of crucial importance in science and engineering. The method of screening may be static or dynamic resulting in steady or unsteady governing models of partial differential equations (PDEs). Also, the host domain in which the obstacle is contained may be bounded, as in the inverse conductivity problem [21], or unbounded, as in inverse scattering problems [9].

Compared to direct problems where the obstacle is known, the associated inverse geometric problem in which the obstacle is unknown is considerably more difficult to solve because it is both non–linear and ill–posed. Theoretically, the issue of the solution's uniqueness is very important as it illustrates what and how many measurements are required to uniquely detect the unknown obstacle. Conditional stability estimates are also very significant as they may highlight where the instability of solution comes from, though numerically this issue is commonly dealt with through regularization. Solving nonlinear obstacle problems involves the iterative

minimization of a certain functional. At each iteration a direct problem needs to be solved and therefore a fast forward solver is desirable. In this framework, meshless methods, such as the method of fundamental solutions (MFS) [28] or the Trefftz method [13, 29] have proved very efficient and easy to implement.

The plan of the paper is as follows. The mathematical formulation of the inverse problem concerning detecting an unknown obstacle submerged in a Stokes flow of steady, incompressible fluid is described in Section 2. Two meshless methods based on the MFS and the Trefftz method are described in Sections 3 and 4, respectively, and numerical results obtained from solving the direct problem (when the obstacle is known) are presented and discussed. Sections 5 and 6 present the implementation of the Trefftz method for solving the nonlinear inverse problem of detecting the unknown obstacle and the corresponding numerical results, respectively. Finally, in Section 7 we present some concluding remarks and suggest some possible future directions of research.

2 Mathematical formulations

It is well–known that in two dimensions, the Stokes equations for a stationary incompressible fluid flowing at low Reynolds numbers reduce to the biharmonic equation for the streamfunction ψ, namely,

$$\Delta^2\psi = 0 \quad \text{in } \Omega \setminus \overline{D}, \tag{1}$$

where the fluid velocity components are given by $u = \partial\psi/\partial y$ and $v = -\partial\psi/\partial x$ and D represents an obstacle immersed in the domain Ω.

We consider the inverse geometric problem formulated by Ramm [37], which requires identifying a zero–level set contour $\partial D = \Gamma \subset \overline{\Omega}$ such that

$$\psi = 0 \quad \text{over } \Gamma, \tag{2}$$

where the unbounded fluid domain is $\Omega = \mathbb{R} \times (-\infty, h),\ h > 0$, from the Cauchy data measurements on the upper boundary $\mathbb{R} \times \{h\}$, namely,

$$\psi(x,h) = f_1(x), \quad \frac{\partial\psi}{\partial y}(x,h) = f_2(x), \quad x \in \mathbb{R}, \tag{3}$$

$$\Delta\psi(x,h) = f_3(x), \quad \frac{\partial(\Delta\psi)}{\partial y}(x,h) = f_4(x), \quad x \in \mathbb{R}, \tag{4}$$

where $\omega = \Delta\psi$ represents the fluid vorticity and f_i, $i = \overline{1,4}$, $f_1 \not\equiv 0$, are known functions, which are assumed to decay sufficiently fast at $\pm\infty$ to ensure the uniqueness of the solution. The inverse geometric problem mentioned above in (1)–(4) can also be formulated in the context of Kirchhoff's plate elasticity in which ψ represents the deflection of a plate and ω the bending moment. The case when Ω is a bounded domain, $\Gamma \subset \partial\Omega$ and the data (3) and (4) are given on $\partial\Omega \setminus \Gamma$, was investigated in [41] using the MFS. In the current paper we investigate the case when $\Omega = \mathbb{R} \times (-\infty, h)$ is an unbounded domain and $\Gamma \subset \Omega$ is a simply–connected closed contour enclosing an unknown immersed object $D \subset \Omega$, see Figure 1.

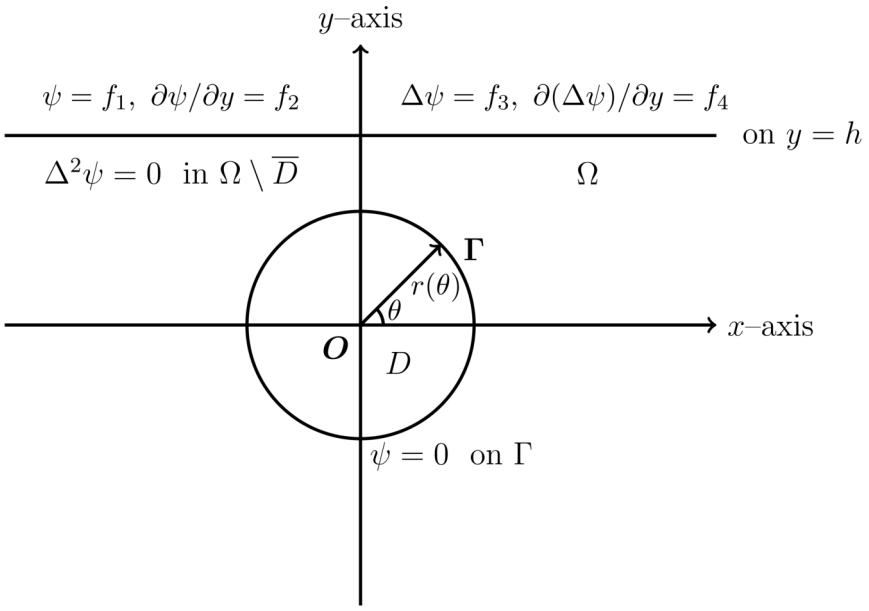

Figure 1: Schematic diagram for geometry and boundary conditions for the inverse problem.

A similar inverse problem on the identification of a rigid body immersed in a Stokes flow occupying a bounded domain from boundary fluid velocity and traction measurements was considered in [1, 2, 35]. However, in our inverse formulation, in equations (3) and (4) the Cauchy data are given in terms of the streamfunction f_1, the slope of the streamfunction f_2, the vorticity f_3 and the the slope of the vorticity f_4. Note that the boundary condition (2) is physically expressing that the boundary Γ of the obstacle D is a streamline. Ramm [37] gave a counter–example for which the solution of the inverse problem (1)-(4) does not exist. However, in this study we shall assume that the solution of the problem always exists. The issue of uniqueness of the solution is still under investigation. The problem (1)-(4) is still ill–posed since small errors in the input data (3) and/or (4) cause large deviations in the solution ψ.

In the course of solving the inverse problem we may also need the solution of the direct problem given by the biharmonic equation (1) subject to the boundary conditions

$$\psi = 0, \quad \Delta\psi = g \quad \text{on } \Gamma = \partial D, \tag{5}$$

$$\psi(x, h) = f_1(x), \quad \Delta\psi(x, h) = f_3(x), \quad x \in \mathbb{R}, \tag{6}$$

where g is a known function representing the specification of the vorticity on the contour Γ of the obstacle D. The problem consisting of equations (1), (5) and (6) can actually be split into a direct Dirichlet problem for Laplace's equation given by

$$\Delta\omega = 0 \qquad \text{in } \Omega \setminus \overline{D}, \tag{7}$$

$$\omega = g \qquad \text{on } \Gamma = \partial D, \tag{8}$$

$$\omega(x, h) = f_3(x), \qquad x \in \mathbb{R}, \tag{9}$$

and a direct Dirichlet problem for Poisson's equation given by

$$\Delta\psi = \omega \qquad \text{in } \Omega \setminus \overline{D}, \tag{10}$$

$$\psi = 0 \qquad \text{on } \Gamma = \partial D, \tag{11}$$

$$\psi(x, h) = f_1(x), \qquad x \in \mathbb{R}. \tag{12}$$

For the solution of the inverse geometric problem (1)-(4) we develop the MFS and the Trefftz

method, which, due to their meshless nature, possess certain advantages over traditional domain or boundary discretization methods [8]. Note that the application of the boundary element method (BEM) to the biharmonic equation in unbounded two–dimensional domains $\Omega \setminus \overline{D}$ is not straightforward due to the appearance of the Stokes paradox, see [11]. For the development of the MFS for some other inverse boundary value problems for the biharmonic equation in bounded domains see [34, 41].

3 The method of fundamental solutions (MFS)

All the applications of the MFS for the biharmonic equation have so far been for bounded domains $\Omega \subset \mathbb{R}^d$. More specifically, various MFS formulations may be found in [15, 25–27, 33], and in all the MFS uses the fundamental solution of the biharmonic operator Δ^2 given by

$$E_2(\mathbf{x};\boldsymbol{\xi}) = \begin{cases} |\mathbf{x}-\boldsymbol{\xi}|^2 \ln|\mathbf{x}-\boldsymbol{\xi}|, & \text{in two dimensions } (d=2), \\ |\mathbf{x}-\boldsymbol{\xi}|, & \text{in three dimensions } (d=3), \end{cases} \tag{13}$$

where the multiplying constant $1/(8\pi)$ has been omitted since it is incorporated in the unknown coefficients of the approximation, as described below. The traditional MFS biharmonic formulation also employs the fundamental solution of the Laplacian operator Δ given by

$$E_1(\mathbf{x};\boldsymbol{\xi}) = \begin{cases} \ln|\mathbf{x}-\boldsymbol{\xi}|, & \text{in two dimensions } (d=2), \\ |\mathbf{x}-\boldsymbol{\xi}|^{-1}, & \text{in three dimensions } (d=3), \end{cases} \tag{14}$$

where the multiplying constants $-1/(2\pi)$ for $d=2$, and $1/(4\pi)$ for $d=3$, have been omitted for the same reason mentioned above. Let Ω_1 be a domain which compactly contains Ω, i.e. $\overline{\Omega} \subset \Omega_1$, and let us denote by

$$F^1_\Omega(\partial\Omega_1) = \left\{ \left(\int_{\partial\Omega_1} f(\boldsymbol{\xi})\, E_1(\mathbf{x};\boldsymbol{\xi})\, dS(\boldsymbol{\xi}) \right)_{\mathbf{x}\in\Omega} ;\ f \in C^\infty(\partial\Omega_1) \right\},$$

$$F^2_\Omega(\partial\Omega_1) = \left\{ \left(\int_{\partial\Omega_1} \left[f(\boldsymbol{\xi})\, E_1(\mathbf{x};\boldsymbol{\xi}) + g(\boldsymbol{\xi})\, E_2(\mathbf{x};\boldsymbol{\xi}) \right] dS(\boldsymbol{\xi}) \right)_{\mathbf{x}\in\Omega} ;\ f,g \in C^\infty(\partial\Omega_1) \right\},$$

the sets of "single–layer" potentials for the Laplace and biharmonic equations, respectively, when the given boundary values and the sought solution are defined on different curves, see [4, 18, 32, 36]. We also define the sets of harmonic and biharmonic functions in Ω, as

$$P^1_\Omega = \{ u \in H^s(\Omega) \mid \Delta u = 0 \text{ in } \Omega \}, \quad P^2_\Omega = \left\{ u \in H^s(\Omega) \mid \Delta^2 u = 0 \text{ in } \Omega \right\}, \tag{15}$$

where $H^s(\Omega)$ is the usual Sobolev space with $s \in \mathbb{R}$. The following denseness theorem is proved in [4].

Theorem 1 (see Theorem 2.2 of [4])
Let $\Omega \subset \overline{\Omega} \subset \Omega_1 \subset \mathbb{R}^d$ be simply connected bounded domains with smooth boundaries. Then for any $s \in \mathbb{R}$ we have

(i) in $d=3$ dimensions, $F^2_\Omega(\partial\Omega_1)$ is dense in $H^s(\Omega) \cap P^2_\Omega$ in the topology of $H^s(\Omega)$;

(ii) in $d=2$ dimensions, $F^2_\Omega(\partial\Omega_1) \oplus \mathbb{R} \oplus (\mathbb{R}\cdot|\mathbf{x}|^2)$ is dense in $H^s(\Omega) \cap P^2_\Omega$ in the topology of $H^s(\Omega)$, where $\mathbb{R}\cdot|\mathbf{x}|^2 = \{c(x_1^2+x_2^2) \mid c \in \mathbb{R},\ \mathbf{x}=(x_1,x_2) \in \mathbb{R}^2\}$.

In $d = 2$ dimensions, the method of proof of Theorem 1 utilises the following important estimates (valid for $\mathbf{x} \in \Omega$ and $|\boldsymbol{\xi}|$ large) derived using Taylor's series for the function $\ln(1-t)$:

$$|\mathbf{x}-\boldsymbol{\xi}|^2 = \langle \mathbf{x}-\boldsymbol{\xi}, \mathbf{x}-\boldsymbol{\xi}\rangle = |\mathbf{x}|^2 - 2\langle \mathbf{x}, \boldsymbol{\xi}\rangle + |\boldsymbol{\xi}|^2 = |\boldsymbol{\xi}|^2 \left(1 - \frac{2\langle \mathbf{x}, \boldsymbol{\xi}\rangle}{|\boldsymbol{\xi}|^2} + \frac{|\mathbf{x}|^2}{|\boldsymbol{\xi}|^2}\right),$$

$$\ln|\mathbf{x}-\boldsymbol{\xi}| = \ln|\boldsymbol{\xi}| + \frac{1}{2}\ln\left(1 - \frac{2\langle \mathbf{x}, \boldsymbol{\xi}\rangle}{|\boldsymbol{\xi}|^2} + \frac{|\mathbf{x}|^2}{|\boldsymbol{\xi}|^2}\right) = \ln|\boldsymbol{\xi}| + O\left(\frac{1}{|\boldsymbol{\xi}|}\right),$$

$$|\mathbf{x}-\boldsymbol{\xi}|^2 \ln|\mathbf{x}-\boldsymbol{\xi}| = \left(|\mathbf{x}|^2 + |\boldsymbol{\xi}|^2\right)\ln|\boldsymbol{\xi}| - (2|\boldsymbol{\xi}|\ln|\boldsymbol{\xi}| + 1)\langle \mathbf{x}, \boldsymbol{\xi}\rangle + \frac{\langle \mathbf{x}, \boldsymbol{\xi}\rangle^2}{|\boldsymbol{\xi}|^2} + \frac{1}{2}|\mathbf{x}|^2 + O\left(\frac{1}{|\boldsymbol{\xi}|}\right).$$

It also uses the fact that that the functions x_1, x_2, x_1x_2 and $x_1^2 - x_2^2$ belong to $F^1_\Omega(\partial\Omega_1) \subset F^2_\Omega(\partial\Omega_1)$, and this is a reason why the first single–layer potential in the definition of the set $F^2_\Omega(\partial\Omega_1)$ needs to be included. One can also get the functions 1 and $|\mathbf{x}|^2$ to be in $F^2_\Omega(\partial\Omega_1)$ by ensuring that $\partial\Omega_1$ does not coincide with the contours of logarithmic capacity 1 and e^{-1}, see [14]. Further, in [4] it is stated that Theorem 1 remains valid for more complicated domains Ω which may be unbounded, multiconnected or may include holes.

In the traditional MFS formulation, the solution ψ of the two–dimensional biharmonic equation (1) is approximated by a linear combination of fundamental solutions of the form, see [4].

$$\psi_M(\mathbf{c}, \mathbf{d}, \mathbf{x}) = \sum_{j=1}^{2M} \left[c_j\, E_1(\mathbf{x}; \boldsymbol{\xi}^j) + d_j\, E_2(\mathbf{x}; \boldsymbol{\xi}^j)\right], \quad \mathbf{x} \in \overline{\Omega} \setminus D, \tag{16}$$

where $\mathbf{c} = [c_1, c_2, ..., c_M]$ and $\mathbf{d} = [d_1, d_2, ..., d_M]$ are unknown real coefficients, the $2M = \mathrm{M}$ source points (or *singularities*) $\boldsymbol{\xi}^j \in \mathbb{R}^2 \setminus \overline{\Omega}$ for $j = \overline{1, M}$, and $\boldsymbol{\xi}^j \in D$ for $j = \overline{(M+1), 2M}$, and E_1 and E_2 denote the fundamental solutions for the two–dimensional Laplace and the biharmonic operators, respectively, see (13) and (14),

$$E_1(\mathbf{x}; \boldsymbol{\xi}^j) = \ln|\mathbf{x} - \boldsymbol{\xi}^j|, \qquad E_2(\mathbf{x}; \boldsymbol{\xi}^j) = |\mathbf{x} - \boldsymbol{\xi}^j|^2 \ln|\mathbf{x} - \boldsymbol{\xi}^j|. \tag{17}$$

Clearly, we also have the corresponding MFS approximation of the vorticity

$$\omega_M(\mathbf{c}, \mathbf{d}, \mathbf{x}) = \sum_{j=1}^{2M} d_j\, \Delta E_2(\mathbf{x}; \boldsymbol{\xi}^j), \quad \mathbf{x} \in \overline{\Omega} \setminus D. \tag{18}$$

Therefore, from (3), (4) and (16), we have

$$f_1(x) = \sum_{j=1}^{2M} \left[c_j\, E_1(x, h; \boldsymbol{\xi}^j) + d_j\, E_2(x, h; \boldsymbol{\xi}^j)\right], \quad x \in \mathbb{R}, \tag{19}$$

$$f_2(x) = \sum_{j=1}^{2M} \left[c_j \frac{\partial E_1}{\partial y}(x, h; \boldsymbol{\xi}^j) + d_j \frac{\partial E_2}{\partial y}(x, h; \boldsymbol{\xi}^j)\right], \quad x \in \mathbb{R}, \tag{20}$$

$$f_3(x) = \sum_{j=1}^{2M} d_j\, \Delta E_2(x, h; \boldsymbol{\xi}^j), \quad x \in \mathbb{R}, \tag{21}$$

$$f_4(x) = \sum_{j=1}^{2M} d_j \frac{\partial(\Delta E_2)}{\partial y}(x, h; \boldsymbol{\xi}^j), \quad x \in \mathbb{R}, \tag{22}$$

where $\boldsymbol{\xi}^j = (\xi_1^j, \xi_2^j)$ and

$$\frac{\partial E_1}{\partial y}(x,h;\boldsymbol{\xi}^j) = \frac{h-\xi_2^j}{|(x,h)-\boldsymbol{\xi}^j|^2}\,, \qquad \frac{\partial E_2}{\partial y}(x,h;\boldsymbol{\xi}^j) = (h-\xi_2^j)\left\{1+\ln|(x,h)-\boldsymbol{\xi}^j|^2\right\},$$

$$\Delta E_2(x,h;\boldsymbol{\xi}^j) = 4\left[1+\ln|(x,h)-\boldsymbol{\xi}^j|\right], \qquad \frac{\partial(\Delta E_2)}{\partial y}(x,h;\boldsymbol{\xi}^j) = \frac{4(h-y_2^j)}{|(x,h)-\boldsymbol{\xi}^j|^2}\,.$$

3.1 MFS results for the direct problem given by equations (1), (5) and (6)

In this subsection, we employ the MFS to solve the direct problem given by equations (1), (5) and (6) where Γ is the boundary of the disk

$$D = \left\{(x,y)\in\mathbb{R}^2 \,|\, x^2+y^2 < R_0^2\right\}, \qquad R_0 = 0.6, \tag{23}$$

with the data (5) and (6) specified by

$$\psi = 0, \qquad \omega = \Delta\psi = g = 4 \;\text{ on }\; \Gamma = \partial D, \tag{24}$$

$$\begin{aligned}
&\psi(x,h) = f_1(x) = \left(\frac{x^2+1}{2}\right)\ln\left(\frac{x^2+1}{R_0^2}\right),\\
&\omega(x,h) = \Delta\psi(x,h) = f_3(x) = 4\left[1+\frac{1}{2}\ln\left(\frac{x^2+1}{R_0^2}\right)\right], \quad x\in\mathbb{R},
\end{aligned} \tag{25}$$

where $h = 1$. Then the direct problem governed by the biharmonic equation (1) subjected to (24) and (25) has the analytical solution

$$\psi(x,y) = \frac{1}{2}\left(x^2+y^2\right)\ln\left(\frac{x^2+y^2}{R_0^2}\right), \quad (x,y)\in\Omega\setminus\overline{D}, \tag{26}$$

which can be verified by direct substitution.

Considering polar coordinates $x = r\cos(\theta)$, $y = r\sin(\theta)$, $r = \sqrt{x^2+y^2}$, when evaluating the normal derivatives $\partial\psi_M/\partial n = -\partial\psi_M/\partial r$ and $\partial\omega_M/\partial n = -\partial\omega_M/\partial r$ on the boundary Γ of the disk (23), we also need the following expressions:

$$\begin{aligned}
\frac{\partial E_1}{\partial r}(\mathbf{x};\boldsymbol{\xi}^j) &= \frac{\partial E_1}{\partial x}(\mathbf{x};\boldsymbol{\xi}^j)\,\frac{\partial x}{\partial r} + \frac{\partial E_1}{\partial y}(\mathbf{x};\boldsymbol{\xi}^j)\,\frac{\partial y}{\partial r}\\
&= \frac{(x-\xi_1^j)}{|\mathbf{x}-\boldsymbol{\xi}^j|^2}\,\frac{x}{\sqrt{x^2+y^2}} + \frac{(y-\xi_2^j)}{|\mathbf{x}-\boldsymbol{\xi}^j|^2}\,\frac{y}{\sqrt{x^2+y^2}} = \frac{(x-\xi_1^j)\,x+(y-\xi_2^j)\,y}{|\mathbf{x}-\boldsymbol{\xi}^j|^2\,\sqrt{x^2+y^2}},
\end{aligned}$$

where $\mathbf{x} = (x,y)$ and $\boldsymbol{\xi}^j = (\xi_1^j, \xi_2^j)$,

$$\begin{aligned}
\frac{\partial E_2}{\partial r}(\mathbf{x};\boldsymbol{\xi}^j) &= \frac{\partial E_2}{\partial x}(\mathbf{x};\boldsymbol{\xi}^j)\,\frac{\partial x}{\partial r} + \frac{\partial E_2}{\partial y}(\mathbf{x};\boldsymbol{\xi}^j)\,\frac{\partial y}{\partial r}\\
&= (x-\xi_1^j)\left(1+\ln(|\mathbf{x}-\boldsymbol{\xi}^j|^2)\right)\,\frac{x}{\sqrt{x^2+y^2}} + (y-\xi_2^j)\left(1+\ln(|\mathbf{x}-\boldsymbol{\xi}^j|^2)\right)\,\frac{y}{\sqrt{x^2+y^2}}\\
&= \frac{\left((x-\xi_1^j)\,x+(y-\xi_2^j)\,y\right)\left(1+\ln(|\mathbf{x}-\boldsymbol{\xi}^j|^2)\right)}{\sqrt{x^2+y^2}},
\end{aligned}$$

$$\frac{\partial(\Delta E_2)}{\partial r}(\mathbf{x};\boldsymbol{\xi}^j) = \frac{\partial(\Delta E_2)}{\partial x}(\mathbf{x};\boldsymbol{\xi}^j)\,\frac{\partial x}{\partial r} + \frac{\partial(\Delta E_2)}{\partial y}(\mathbf{x};\boldsymbol{\xi}^j)\,\frac{\partial y}{\partial r}$$
$$= \frac{4(x-\xi_1^j)}{|\mathbf{x}-\boldsymbol{\xi}^j|^2}\,\frac{x}{\sqrt{x^2+y^2}} + \frac{4(y-\xi_2^j)}{|\mathbf{x}-\boldsymbol{\xi}^j|^2}\,\frac{y}{\sqrt{x^2+y^2}} = \frac{4\left((x-\xi_1^j)\,x + (y-\xi_2^j)\,y\right)}{|\mathbf{x}-\boldsymbol{\xi}^j|^2\,\sqrt{x^2+y^2}}.$$

On the sub-boundary $y = h = 1$, we choose the boundary collocation points $\mathbf{x}^i$, $i = \overline{1,N}$, and the outer source points $\boldsymbol{\xi}^j$, $j = \overline{1,M}$, as

$$\mathbf{x}^i = (x^i, 1), \quad x^i = -L + \frac{2(i-1)L}{N-1}, \quad i = \overline{1,N}, \tag{27}$$

$$\boldsymbol{\xi}^j = (\xi_1^j, 1+\delta), \quad \xi_1^j = -L + \frac{2(j-1)L}{M-1}, \quad j = \overline{1,M}, \tag{28}$$

where $L > 0$ is a sufficiently large number such as $L = 10$ to approximate the infinite real axis by the finite interval $x \in (-L, L) = (-10, 10)$, and $\delta > 0$ is a parameter to be specified. We also choose the boundary collocation points $\mathbf{x}^{N+k} \in \Gamma$ for $k = \overline{1,M}$, and the inner source points $\boldsymbol{\xi}^{M+k} \in D$ for $k = \overline{1,M}$, as

$$\mathbf{x}^{N+k} = R_0\left(\cos(\theta_k), \sin(\theta_k)\right), \quad \boldsymbol{\xi}^{M+k} = \eta\,\mathbf{x}^{N+k}, \quad k = \overline{1,M}, \tag{29}$$

where $\eta \in (0,1)$ is chosen to be neither too small nor too large [31], and $\theta_k = \dfrac{2\pi(k-1)}{M}$ for $k = \overline{1,M}$. The resulting MFS system of $(2N+2M)$ linear equations in $4M$ unknowns is given by

$$\psi_M(\mathbf{c},\mathbf{d},\mathbf{x}^i) = f_1(x^i), \quad i = \overline{1,N}, \tag{30}$$

$$\Delta\psi_M(\mathbf{c},\mathbf{d},\mathbf{x}^i) = f_3(x^i), \quad i = \overline{1,N}, \tag{31}$$

$$\psi_M(\mathbf{c},\mathbf{d},\mathbf{x}^{N+k}) = 0, \quad \omega_M = \Delta\psi_M(\mathbf{c},\mathbf{d},\mathbf{x}^{N+k}) = g(\mathbf{x}^{N+k}), \quad k = \overline{1,M}, \tag{32}$$

where for a unique solution we require $N \geq M$. We may rewrite the system of equations (30)–(32) in generic form

$$A\,\mathbf{a} = \mathbf{b}, \tag{33}$$

where $\mathbf{a} = [\mathbf{c},\mathbf{d}]^{\mathrm{T}}$, $\mathbf{b} = \left[\left(f_1(x^i)\right)_{i=\overline{1,N}}, \left(f_3(x^i)\right)_{i=\overline{1,N}}, \mathbf{0}, \left(g(\mathbf{x}^{N+k})\right)_{k=\overline{1,M}}\right]^{\mathrm{T}}$,

$$A = \begin{bmatrix} E_1(\mathbf{x}^i;\boldsymbol{\xi}^j) & E_2(\mathbf{x}^i;\boldsymbol{\xi}^j) \\ \mathbf{0} & \Delta E_2(\mathbf{x}^i;\boldsymbol{\xi}^j) \\ E_1(\mathbf{x}^{N+k};\boldsymbol{\xi}^j) & E_2(\mathbf{x}^{N+k};\boldsymbol{\xi}^j) \\ \mathbf{0} & \Delta E_2(\mathbf{x}^{N+k};\boldsymbol{\xi}^j) \end{bmatrix}, \quad i = \overline{1,N},\ j,k = \overline{1,M}.$$

The system of linear equations (33) depends on N, M, δ and η and is poorly–conditioned, [5]. After extensive experimentation with these parameters, we report results obtained with $N = M = 40$, $\eta = 0.56$ and $\delta = 1.34$, which yield a condition number 5.5×10^8 for the matrix A in (33).

The numerical results are compared with the exact solutions in Figures 2–4. The ψ_M and ω_M values are computed at the midpoints between the collocation points on the upper boundary $y = h = 1$ and on the inner boundary $r = R_0 = 0.6$. Streamfunction and vorticity results are in excellent agreement with the exact solutions given by

$$\omega(x,y) = \Delta\psi(x,y) = 2\ln\left(\frac{x^2+y^2}{R_0^2}\right) + 4, \quad (x,y) \in \Omega \setminus \overline{D}, \tag{34}$$

$$\frac{\partial \psi}{\partial y}(x,1) = f_2(x) = \ln\left(\frac{x^2+1}{R_0^2}\right) + 1, \quad x \in \mathbb{R}, \tag{35}$$

$$\frac{\partial \omega}{\partial y}(x,1) = \frac{\partial(\Delta\psi)}{\partial y}(x,1) = f_4(x) = \frac{4}{x^2+1}, \quad x \in \mathbb{R}, \tag{36}$$

$$\frac{\partial \psi}{\partial r}(x,y)\bigg|_{r=R_0} = \sqrt{x^2+y^2}\left[1 + \ln\left(\frac{x^2+y^2}{R_0^2}\right)\right] = R_0, \quad (x,y) \in \Gamma, \tag{37}$$

$$\frac{\partial \omega}{\partial r}(x,y)\bigg|_{r=R_0} = \frac{4}{\sqrt{x^2+y^2}} = \frac{4}{R_0}, \quad (x,y) \in \Gamma, \tag{38}$$

with the obtained results being graphically indistinguishable. However, the accuracy of the MFS drops visibly in the computation of the derivatives on the boundaries $\{(x,h) \mid x \in \mathbb{R}\} \cup \Gamma$ and the streamfunction inside the domain $\Omega \setminus \overline{D}$.

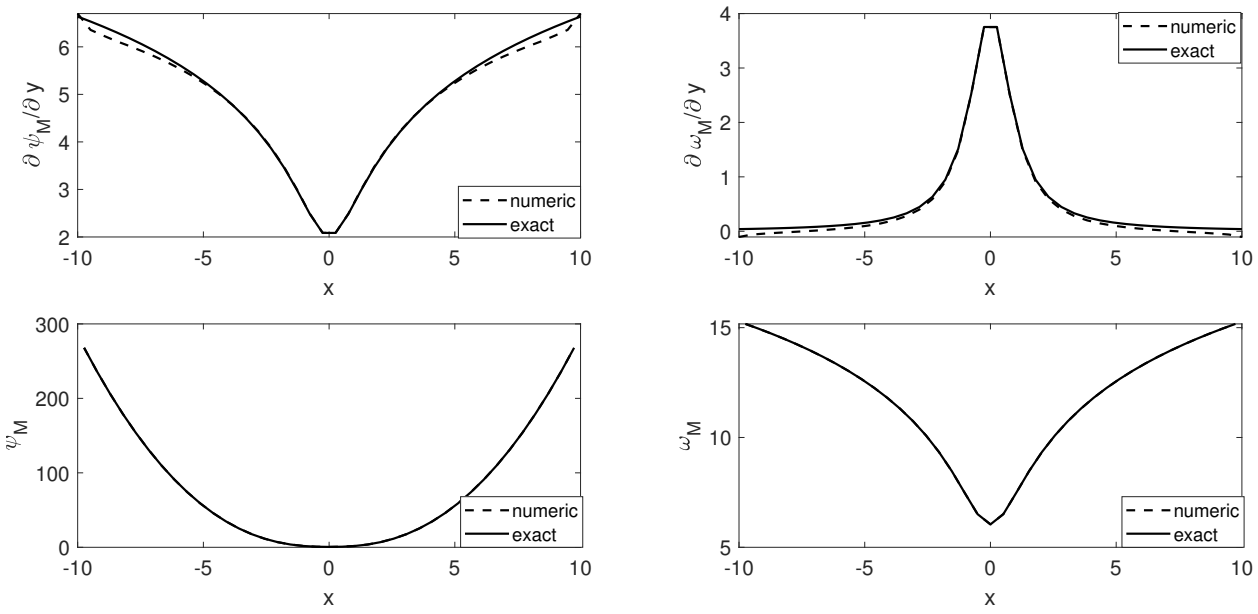

Figure 2: MFS approximations of the direct problem (1), (5) and (6) on the upper boundary $y = h = 1$, as functions of $x \in (-L, L) = (-10, 10)$, in comparison with the exact solutions (26) and (34)-(36).

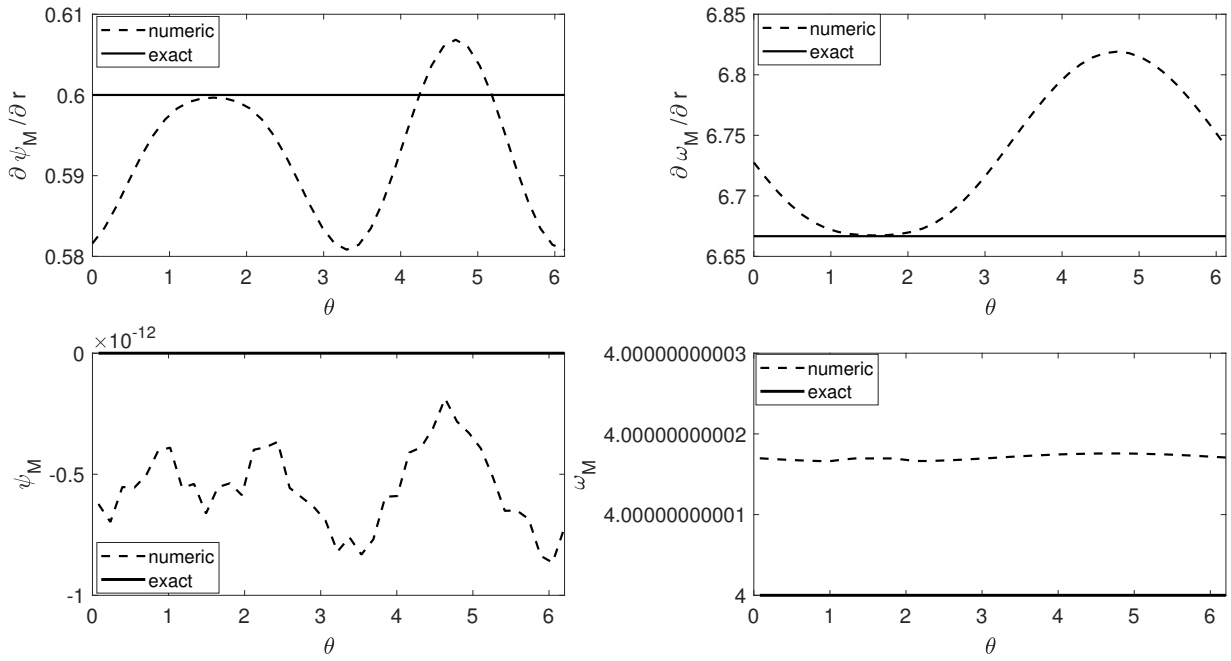

Figure 3: MFS approximations of the direct problem (1), (5) and (6) on the inner boundary $r = R_0 = 0.6$, as functions of $\theta \in [0, 2\pi)$, in comparison with the exact solutions (26), (34), (37) and (38).

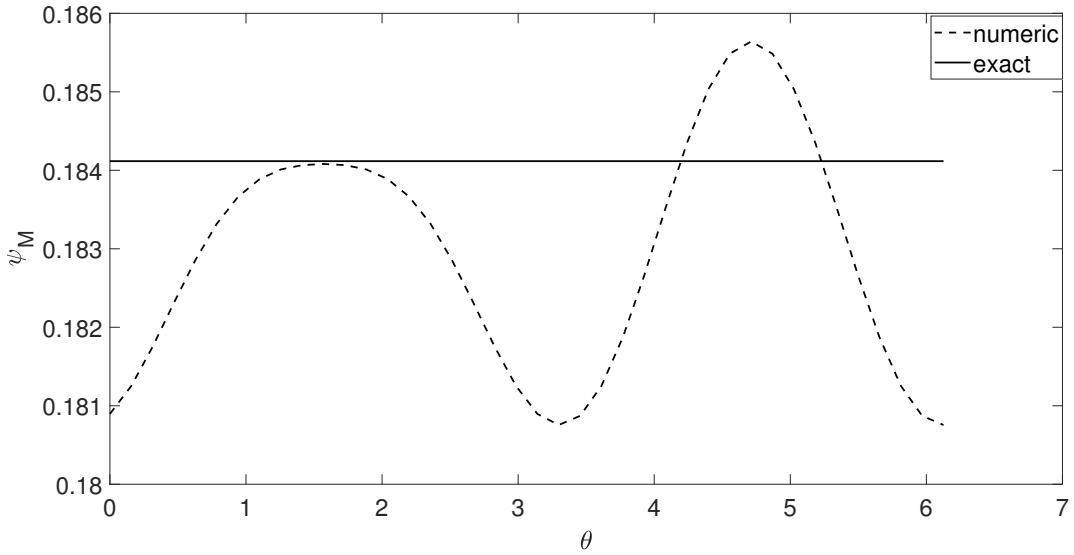

Figure 4: MFS approximation of the direct problem (1), (5) and (6) on the interior circle $r = 0.8$, as a function of $\theta \in [0, 2\pi)$, in comparison with the exact solution (26).

4 The Trefftz method

An alternative to the MFS is the Trefftz method which is also meshless and, like the MFS, possesses certain advantages over traditional domain or boundary discretization methods [19].

Notable, it requires neither domain nor boundary discretisation and does not involve numerical integration. Furthermore, Trefftz complete functions are very effective for infinite domain problems. For bounded simply–connected and annular domains, as well as for unbounded exterior domains, the equivalence between the Trefftz method and the MFS for the Laplace and biharmonic equations has been discussed in [6, 7] and [38], respectively. Moreover, the Trefftz method has been successfully applied to a variety of direct plane elasticity and Kirchhoff plate bending problems, see [23, 24].

Following [30], we approximate the streamfunction as if $\Omega \setminus \overline{D}$ were a bounded annulus by the following expansion of biharmonic functions:

$$\begin{aligned}\psi_{\mathrm{N}}(\mathbf{e}, r, \theta) = \alpha_0 + \gamma_0\, r^2 + \sum_{n=1}^{\mathrm{N}} r^n \, \left(\alpha_n + \gamma_n r^2\right) \cos(n\theta) + \sum_{n=1}^{\mathrm{N}} r^n \, \left(\beta_n + \delta_n r^2\right) \sin(n\theta) \\ + \left(\epsilon_0 + \eta_0 r^2\right) \ln(r) + \sum_{n=1}^{\mathrm{N}} r^{-n} \, \left(\epsilon_n + \eta_n r^2\right) \cos(n\theta) + \sum_{n=1}^{\mathrm{N}} r^{-n} \, \left(\zeta_n + \xi_n r^2\right) \sin(n\theta), \end{aligned} \tag{39}$$

where N is the truncation number of an infinite series. The $8\mathrm{N}+4$ unknown coefficients in (39) are arranged in the vector

$$\mathbf{e} = (e)_{j=\overline{1,8\mathrm{N}+4}} = \left((\alpha_k, \gamma_k, \epsilon_k, \eta_k)_{k=\overline{0,\mathrm{N}}}, \, (\beta_k, \delta_k, \zeta_k, \xi_k)_{k=\overline{1,\mathrm{N}}}\right). \tag{40}$$

The various derivatives of the functions involved in the Trefftz approximation (39) required in (3) and (4) are listed in Table 1.

Table 1: Summary of functions and derivatives involved in Trefftz approximation.

Function u	$\partial u/\partial y$	Δu	$\partial(\Delta u)/\partial y$
1	0	0	0
r^2	$2r\sin(\theta)$	4	0
$r^n\cos(n\theta)$	$-nr^{n-1}\sin((n-1)\theta)$	0	0
$r^{n+2}\cos(n\theta)$	$-r^{n+1}((n+1)\sin((n-1)\theta) - \sin((n+1)\theta))$	$4(n+1)r^n\cos(n\theta)$	$-4n(n+1)r^{n-1}\sin((n-1)\theta)$
$r^n\sin(n\theta)$	$nr^{n-1}\cos((n-1)\theta)$	0	0
$r^{n+2}\sin(n\theta)$	$r^{n+1}((n+1)\cos((n-1)\theta) - \cos((n+1)\theta))$	$4(n+1)r^n\sin(n\theta)$	$4n(n+1)r^{n-1}\cos((n-1)\theta)$
$\ln r$	$(1/r)\sin(\theta)$	0	0
$r^2\ln r$	$(2\ln r + 1)r\sin(\theta)$	$4(\ln r + 1)$	$4\sin(\theta)/r$
$r^{-n}\cos(n\theta)$	$-(n/r^{n+1})\sin((n+1)\theta)$	0	0
$r^{2-n}\cos(n\theta)$	$-r^{1-n}(sin((n-1)\theta) + (n-1)\sin((n+1)\theta))$	$-(4/r^n)(n-1)\cos(n\theta)$	$(4/r^{n+1})n(n-1)\sin((n+1)\theta)$
$r^{-n}\sin(n\theta)$	$(n/r^{n+1})\cos((n+1)\theta)$	0	0
$r^{2-n}\sin(n\theta)$	$r^{1-n}(cos((n-1)\theta) + (n-1)\cos((n+1))\theta)$	$-(4/r^n)(n-1)\sin(n\theta)$	$-(4/r^{n+1})n(n-1)\cos((n+1)\theta)$

Another Trefftz method formulation for approximating ψ in the unbounded planar domain $\mathbb{R}^2 \setminus \overline{D}$ is

$$\begin{aligned}\psi_{\mathrm{N}}(\mathbf{f}, r, \theta) =& (a_0 + a_1\, x + a_2\, y)\, \ln(r) + b_0\, r^2\, (\ln(r) - 1) \\ &+ \sum_{n=1}^{\mathrm{N}} r^{-n} \left[(\alpha_n + x\,\gamma_n)\, \cos(n\theta) + (\beta_n + y\,\delta_n)\, \sin(n\theta)\right], \end{aligned} \tag{41}$$

where in polar coordinates $x = r\cos(\theta)$, $y = r\sin(\theta)$ and the vector $\mathbf{f}$ of dimension $4\mathrm{N}+4$ contains the coefficients a_0, a_1, a_2, b_0, $(\alpha_n)_{\overline{1,\mathrm{N}}}$, $(\gamma_n)_{\overline{1,\mathrm{N}}}$, $(\beta_n)_{\overline{1,\mathrm{N}}}$, $(\delta_n)_{\overline{1,\mathrm{N}}}$. Our numerical tests revealed that the Trefftz approximation (39) for the bounded annulus exterior to a simply–connected obstacle is more accurate than (41) for unbounded planar domains. Therefore, in the rest of the analysis we shall only employ the former.

Defining

$$
\begin{aligned}
&G_1(r,\theta)=1, \quad G_2(r,\theta)=r^2, \quad G_3(r,\theta)=\ln(r), \quad G_4(r,\theta)=r^2\ln(r),\\
&P_{1n}(r,\theta)=r^n\cos(n\theta), \quad P_{2n}(r,\theta)=r^2P_{1n}(r,\theta), \quad Q_{1n}(r,\theta)=r^n\sin(n\theta),\\
&Q_{2n}(r,\theta)=r^2Q_{1n}(r,\theta), \quad R_{1n}(r,\theta)=r^{-n}\cos(n\theta), \quad R_{2n}(r,\theta)=r^2R_{1n}(r,\theta),\\
&S_{1n}(r,\theta)=r^{-n}\sin(n\theta), \quad S_{2n}(r,\theta)=r^2S_{1n}(r,\theta),
\end{aligned}
$$

we obtain

$$
\begin{aligned}
\psi_{\mathrm{N}}(\mathbf{e},r,\theta)=\alpha_0\,G_1+\gamma_0\,G_2+\sum_{n=1}^{\mathrm{N}}(\alpha_n\,P_{1n}+\gamma_n\,P_{2n})+\sum_{n=1}^{\mathrm{N}}(\beta_n\,Q_{1n}+\delta_n\,Q_{2n})\\
+\epsilon_0\,G_3+\eta_0\,G_4+\sum_{n=1}^{\mathrm{N}}(\epsilon_n\,R_{1n}+\eta_n\,R_{2n})+\sum_{n=1}^{\mathrm{N}}(\zeta_n\,S_{1n}+\xi_n\,S_{2n})\,. \qquad (42)
\end{aligned}
$$

The streamfunction, vorticity and their normal derivatives on the upper boundary are computed from (42) and

$$
\begin{aligned}
\frac{\partial\psi_{\mathrm{N}}}{\partial y}(\mathbf{e},r,\theta)=\alpha_0\,\frac{\partial G_1}{\partial y}+\gamma_0\,\frac{\partial G_2}{\partial y}+\sum_{n=1}^{\mathrm{N}}\left(\alpha_n\,\frac{\partial P_{1n}}{\partial y}+\gamma_n\,\frac{\partial P_{2n}}{\partial y}\right)+\sum_{n=1}^{\mathrm{N}}\left(\beta_n\,\frac{\partial Q_{1n}}{\partial y}+\delta_n\,\frac{\partial Q_{2n}}{\partial y}\right)\\
+\epsilon_0\,\frac{\partial G_3}{\partial y}+\eta_0\,\frac{\partial G_4}{\partial y}+\sum_{n=1}^{\mathrm{N}}\left(\epsilon_n\,\frac{\partial R_{1n}}{\partial y}+\eta_n\,\frac{\partial R_{2n}}{\partial y}\right)+\sum_{n=1}^{\mathrm{N}}\left(\zeta_n\,\frac{\partial S_{1n}}{\partial y}+\xi_n\,\frac{\partial S_{2n}}{\partial y}\right), \qquad (43)\\
\omega_{\mathrm{N}}(\mathbf{e},r,\theta)=\alpha_0\,\Delta G_1+\gamma_0\,\Delta G_2+\sum_{n=1}^{\mathrm{N}}(\alpha_n\,\Delta P_{1n}+\gamma_n\,\Delta P_{2n})+\sum_{n=1}^{N}(\beta_n\,\Delta Q_{1n}+\delta_n\,\Delta Q_{2n})\\
+\epsilon_0\,\Delta G_3+\eta_0\,\Delta G_4+\sum_{n=1}^{N}(\epsilon_n\,\Delta R_{1n}+\eta_n\,\Delta R_{2n})+\sum_{n=1}^{\mathrm{N}}(\zeta_n\,\Delta S_{1n}+\xi_n\,\Delta S_{2n})\,, \qquad (44)\\
\frac{\partial\omega_{\mathrm{N}}}{\partial y}(\mathbf{e},r,\theta)=\alpha_0\,\frac{\partial(\Delta G_1)}{\partial y}+\gamma_0\,\frac{\partial(\Delta G_2)}{\partial y}+\sum_{n=1}^{\mathrm{N}}\left(\alpha_n\,\frac{\partial(\Delta P_{1n})}{\partial y}+\gamma_n\,\frac{\partial(\Delta P_{2n})}{\partial y}\right)\\
+\sum_{n=1}^{\mathrm{N}}\left(\beta_n\,\frac{\partial(\Delta Q_{1n})}{\partial y}+\delta_n\,\frac{\partial(\Delta Q_{2n})}{\partial y}\right)+\epsilon_0\,\frac{\partial(\Delta G_3)}{\partial y}+\eta_0\,\frac{\partial(\Delta G_4)}{\partial y}\\
+\sum_{n=1}^{\mathrm{N}}\left(\epsilon_n\,\frac{\partial(\Delta R_{1n})}{\partial y}+\eta_n\,\frac{\partial(\Delta R_{2n})}{\partial y}\right)+\sum_{n=1}^{\mathrm{N}}\left(\zeta_n\,\frac{\partial(\Delta S_{1n})}{\partial y}+\xi_n\,\frac{\partial(\Delta S_{2n})}{\partial y}\right), \qquad (45)
\end{aligned}
$$

where (r,θ) are polar coordinate representations of the points $\mathbf{x}=(x,h)$ for $x\in\mathbb{R}$. The Laplacian and the y-derivatives of the T-complete functions were presented in Table 1. Similarly, on the inner boundary ∂D the approximations of the streamfunction, vorticity and their derivatives are given by (42), (44) and

$$
\begin{aligned}
\frac{\partial\psi_{\mathrm{N}}}{\partial r}(\mathbf{e},r,\theta)=\alpha_0\,\frac{\partial G_1}{\partial r}+\gamma_0\,\frac{\partial G_2}{\partial r}+\sum_{n=1}^{\mathrm{N}}\left(\alpha_n\,\frac{\partial P_{1n}}{\partial r}+\gamma_n\,\frac{\partial P_{2n}}{\partial r}\right)+\sum_{n=1}^{\mathrm{N}}\left(\beta_n\,\frac{\partial Q_{1n}}{\partial r}+\delta_n\,\frac{\partial Q_{2n}}{\partial r}\right)\\
+\epsilon_0\,\frac{\partial G_3}{\partial r}+\eta_0\,\frac{\partial G_4}{\partial r}+\sum_{n=1}^{\mathrm{N}}\left(\epsilon_n\,\frac{\partial R_{1n}}{\partial r}+\eta_n\,\frac{\partial R_{2n}}{\partial r}\right)+\sum_{n=1}^{\mathrm{N}}\left(\zeta_n\,\frac{\partial S_{1n}}{\partial r}+\xi_n\,\frac{\partial S_{2n}}{\partial r}\right), \qquad (46)
\end{aligned}
$$

$$\frac{\partial \omega_{\mathrm{N}}}{\partial r}(\mathbf{e}, r, \theta) = \alpha_0 \frac{\partial(\Delta G_1)}{\partial r} + \gamma_0 \frac{\partial(\Delta G_2)}{\partial r} + \sum_{n=1}^{\mathrm{N}} \left(\alpha_n \frac{\partial(\Delta P_{1n})}{\partial r} + \gamma_n \frac{\partial(\Delta P_{2n})}{\partial r} \right)$$
$$+ \sum_{n=1}^{\mathrm{N}} \left(\beta_n \frac{\partial(\Delta Q_{1n})}{\partial r} + \delta_n \frac{\partial(\Delta Q_{2n})}{\partial r} \right) + \epsilon_0 \frac{\partial(\Delta G_3)}{\partial r} + \eta_0 \frac{\partial(\Delta G_4)}{\partial r}$$
$$+ \sum_{n=1}^{\mathrm{N}} \left(\epsilon_n \frac{\partial(\Delta R_{1n})}{\partial r} + \eta_n \frac{\partial(\Delta R_{2n})}{\partial r} \right) + \sum_{n=1}^{\mathrm{N}} \left(\zeta_n \frac{\partial(\Delta S_{1n})}{\partial r} + \xi_n \frac{\partial(\Delta S_{2n})}{\partial r} \right), \tag{47}$$

on $r = R_0$ for $\theta \in [0, 2\pi)$.

4.1 Trefftz method results for the direct problem given by equations (1), (5) and (6)

In this section, we shall apply the Trefftz method based on (39) to the problem described in Section 3.1, previously solved using the MFS. On collocating the boundary condition (6) at the points $(x^i)_{i=\overline{1,N}}$ defined in (27) and the boundary condition (5) at the points $(\mathbf{x}^{N+k})_{k=\overline{1,M}}$ defined in (29), we obtain the following Trefftz system of $2N + 2M$ linear equations in the $8\mathrm{N} + 4$ unknowns involved in the vector $\mathbf{e}$ defined in (40):

$$\psi_{\mathrm{N}}(\mathbf{e}, x^i) = f_1(x^i), \quad i = \overline{1, N}, \tag{48}$$

$$\Delta\psi_{\mathrm{N}}(\mathbf{e}, x^i) = \omega_{\mathrm{N}}(\mathbf{e}, x^i) = f_3(x^i), \quad i = \overline{1, N}, \tag{49}$$

$$\psi_{\mathrm{N}}(\mathbf{e}, \mathbf{x}^{N+k}) = 0, \qquad \omega_{\mathrm{N}}(\mathbf{e}, \mathbf{x}^{N+k}) = g(\mathbf{x}^{N+k}), \quad k = \overline{1, M}. \tag{50}$$

For a unique solution we require $N + M \geq 4\mathrm{N} + 2$ and numerical results are illustrated for $h = 1$, $L = 10$, $R_0 = 0.6$, $N = M = 40$ and $\mathrm{N} = 11$.

The Trefftz approximations for the streamfunction, vorticity and their normal derivatives in comparison with the exact solutions are presented in Figures 5–7. The streamfunction and the vorticity on the boundaries are computed at the midpoints between the boundary collocation points. It can be observed that the Trefftz method solutions are in excellent agreement with the exact solutions.

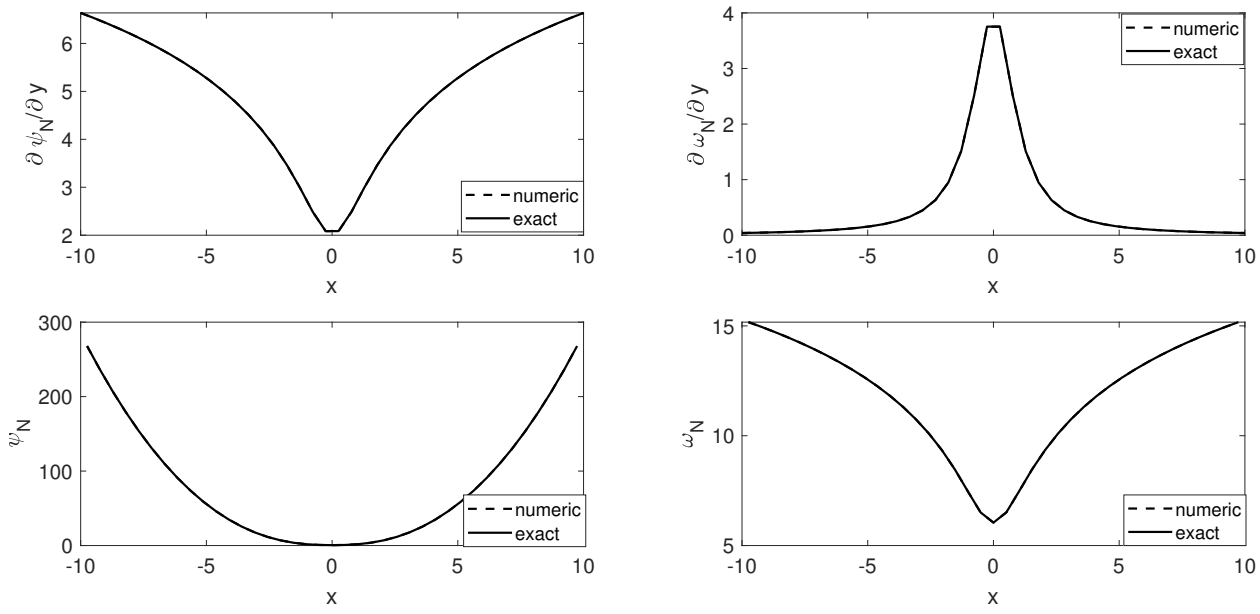

Figure 5: Trefftz method approximations of the direct problem (1), (5) and (6) on the upper boundary $y = h = 1$, as functions of $x \in (-L, L) = (-10, 10)$, in comparison with the exact solutions (26), (34)–(36).

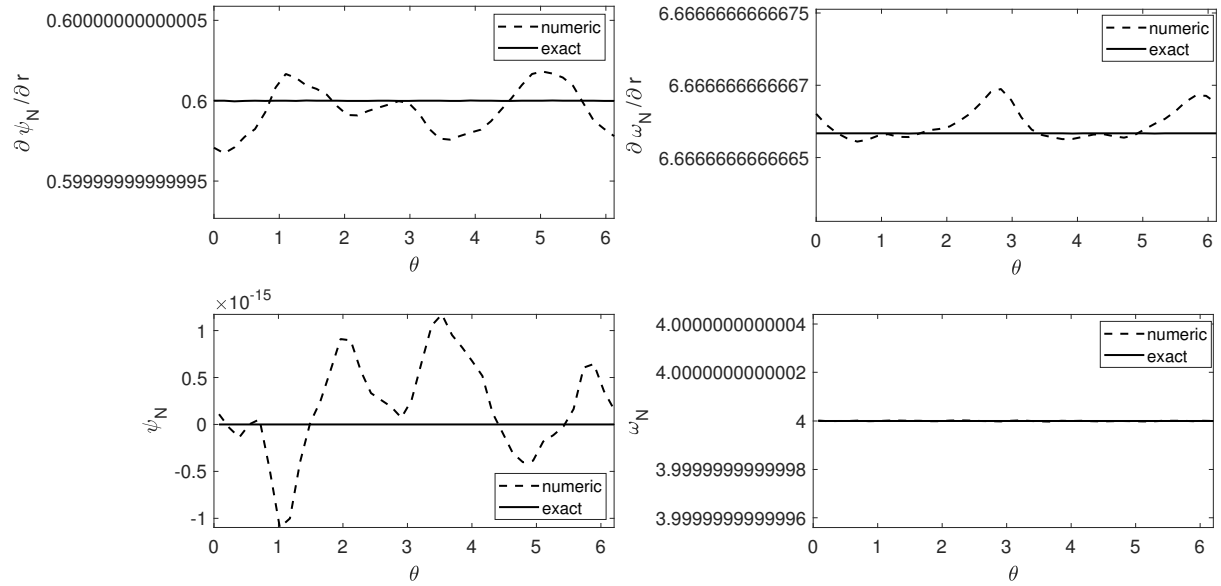

Figure 6: Trefftz method approximations of the direct problem (1), (5) and (6) on the inner boundary $r = R_0 = 0.6$, as functions of $\theta \in [0, 2\pi)$, in comparison with the exact solutions (26), (34), (37) and (38).

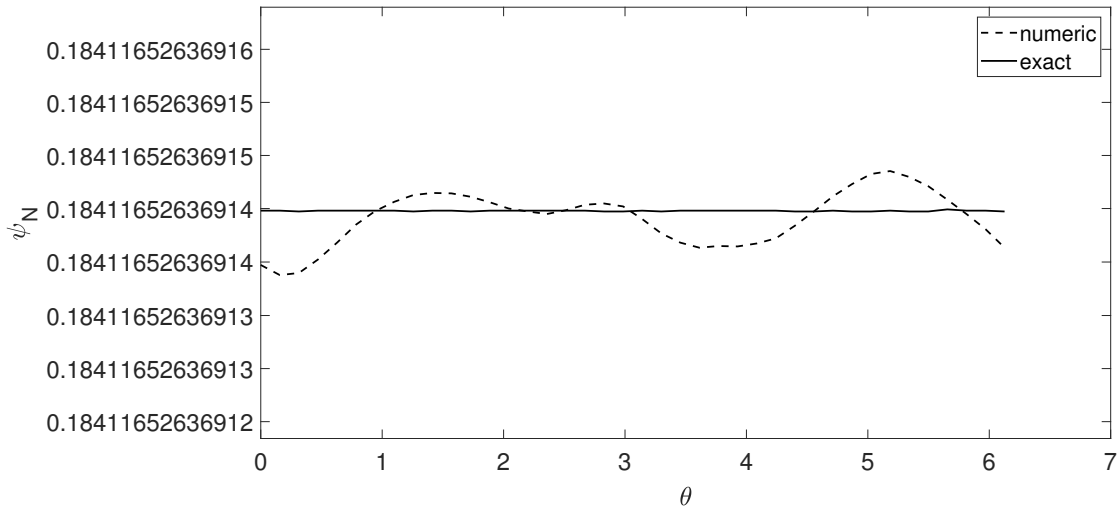

Figure 7: Trefftz method approximation of the direct problem (1), (5) and (6) on the interior circle $r = 0.8$, as a function of $\theta \in [0, 2\pi)$, in comparison with the exact solution (26).

In the next section, we discuss the implementation of the Trefftz method for solving the inverse problem when the obstacle D is unknown.

5 The inverse problem

In the inverse problem, we seek the boundary of the unknown obstacle D that is submerged in the region Ω. On the upper boundary $y = h$ we have the measured data of the streamfunction, vorticity and their normal derivatives. Our aim is to find a contour $\partial D = \Gamma$ inside the region Ω where the streamfunction vanishes. We employ regularized least–squares minimization with the Trefftz method to solve the inverse problem defined by

$$\Delta^2 \psi = 0 \qquad \text{in } \Omega \setminus \overline{D}, \tag{51}$$

$$\psi(x,h) = f_1(x), \quad \frac{\partial \psi}{\partial y}(x,h) = f_2(x), \quad \omega(x,h) = f_3(x), \quad \frac{\partial \omega}{\partial y}(x,h) = f_4(x), \quad x \in \mathbb{R}, \tag{52}$$

$$\psi = 0 \quad \text{over} \quad \Gamma, \tag{53}$$

where f_1 and f_3 are as in the equation (25) and f_2 and f_4 are defined by equations (35) and (36), respectively.

5.1 Representation of the unknown boundary Γ

We assume that the unknown obstacle D is a star–shaped domain with respect to the origin. Thus, we can represent its boundary Γ in polar coordinates as

$$\Gamma: \quad x = r(\theta)\cos\theta, \quad y = r(\theta)\sin(\theta), \quad \theta \in [0, 2\pi), \tag{54}$$

where r is a 2π-periodic function. On discretizing Γ we have

$$r_k = r(\theta_k), \quad \theta_k = \frac{2\pi(k-1)}{M}, \quad k = \overline{1, M}, \tag{55}$$

and we then choose the boundary collocation points $\mathbf{x}^{N+j} \in \Gamma$, $j = \overline{1, M}$, as

$$\mathbf{x}^{N+j} = (r_j \cos(\theta_j), r_j \sin(\theta_j)), \quad j = \overline{1, M}. \tag{56}$$

5.2 Regularized least–squares minimization

In the Trefftz expansion (39) there are $8\mathrm{N}+4$ unknown coefficients $(\alpha_k, \gamma_k, \epsilon_k, \eta_k)_{k=\overline{0,N}}$ and $(\beta_k, \delta_k, \zeta_k, \xi_k)_{k=\overline{1,N}}$, and to these we now add the M unknowns $(r_k)_{k=\overline{1,M}}$ for the polar radius in (55). The above $8\mathrm{N}+\mathrm{M}+4$ unknowns can be determined by imposing the boundary conditions (2)–(4) in a least–squares sense which leads to minimizing the following functional:

$$\begin{aligned} S(\mathbf{e},\mathbf{r}) := \sum_{i=1}^{N} \Big[& \left\{\psi_{\mathrm{N}}(\mathbf{e},\mathbf{x}^i) - f_1(\mathbf{x}^i)\right\}^2 + \left\{\frac{\partial \psi_{\mathrm{N}}}{\partial y}(\mathbf{e},\mathbf{x}^i) - f_2(\mathbf{x}^i)\right\}^2 \\ & + \left\{\Delta\psi_{\mathrm{N}}(\mathbf{e},\mathbf{x}^i) - f_3(\mathbf{x}^i)\right\}^2 + \left\{\frac{\partial (\Delta\psi_{\mathrm{N}})}{\partial y}(\mathbf{e},\mathbf{x}^i) - f_4(\mathbf{x}^i)\right\}^2 \Big] \\ & + \sum_{k=N+1}^{N+M} \left[\psi_{\mathrm{N}}(\mathbf{e},\mathbf{x}^k)\right]^2 + \lambda \left[\sum_{i=1}^{8\mathrm{N}+4} e_i^2 + \sum_{k=1}^{M} (r_k - r_{k-1})^2\right], \end{aligned} \tag{57}$$

where $r_0 := r_N$ and $\lambda \geq 0$ is a regularization parameter to be prescribed [39]. The penalty term containing the parameter λ has been included in (57) in order to improve the stability of solution. Also, the slopes f_2 and f_4 come from practical measurements, which are inherently contaminated with noisy errors, and therefore, in (57) we replace f_2 and f_4 by

$$f_\ell^{(\mathrm{p})}(\mathbf{x}^i) = (1 + \rho_i\, \mathrm{p})\, f_\ell(\mathbf{x}^i), \quad i = \overline{1,N}, \quad \ell = 2, 4, \tag{58}$$

where p represents the percentage of noise and ρ_i for $i = \overline{1,N}$, are pseudo–random numbers drawn from a uniform distribution in $(-1,1)$ using the MATLAB® `rand` routine.

The minimization of the functional (57) subject to the simple bounds on the variables (ensuring that $D \subset \Omega = \{(x,y) | x \in \mathbb{R},\ y \in (-\infty, h)\}$),

$$0 < r_k < \frac{h}{|\sin(\theta_k)|}, \quad k = \overline{1,M}, \tag{59}$$

and $\mathbf{10^{-10}} \leq \mathbf{e} \leq \mathbf{10^{10}}$, is performed iteratively using the MATLAB® routine `lsqnonlin` which is based on trust–region–reflective algorithm. In the routine, `Step Tolerance` and `Function Tolerance` are set to 10^{-25}. Note that if $k \in \{1, \frac{M}{2}+1\}$ in the above expression, we take the right–hand side upper bound to be a large number such as 10^{10}. The initial guess is arbitrary, such as $\mathbf{e}^{(0)} = \mathbf{0}$ and $\mathbf{r}^{(0)} = \mathbf{0.8}h$. We also take $h = 1$, $L = 10$, $N = 100$, $M = 48$ and $\mathrm{N} = 9$. Extensive trial and error computations for various numbers of Trefftz functions N in (39) and numbers of boundary collocation points N and M in (48)–(50) have been performed to determine suitable values that can be selected to illustrate typical numerical results. Nevertheless, more rigorous machine learning choices and error analysis need to be undertaken in the future. For the choice of the regularization parameter λ in (57) we choose the smallest $\lambda \geq 0$ for which a free of oscillations stable solution is obtained [10]. More rigorous criteria, for example based on the discrepancy principle [12] or the L-curve method [17], could also be employed. All computations have been carried out in MATLAB® on a 16GB RAM computer with Intel® Core® i7 processor.

6 Numerical results and discussion for the inverse problem

Figure 8 displays the decreasing convergent behavior of the logarithmic scaled functional values of $S(\mathbf{e},\mathbf{r})$ given by the equation (57), as a function of the number of iterations of the `lsqnonlin`

MATLAB® routine for various regularization parameters $\lambda \in \{0, 10^{-12}, 10^{-6}, 10^{-3}\}$ in case the data (58) is noiseless, i.e. p = 0 in (58). The detected objects at various iterations in the no regularization case ($\lambda = 0$) are visualized in Figure 9. The algorithm converges as the iteration number increases to a shape that is a reasonable approximation of the exact circle of radius $R_0 = 0.6$.

In Figure 10, the detected objects after 400 iterations for various regularization parameters λ are compared with the exact disk. From this figure it can be seen that when $\lambda = 10^{-12}$ and 10^{-6} symmetric artifacts are present which are, however, removed when $\lambda = 10^{-3}$.

Figure 11 shows the convergence of the objective function (57) with $\lambda = 10^{-3}$, when p $\in \{0, 0.1\%, 1\%\}$ noise is included in the data (58). Compared to Figure 8 many more iterations are run in Figure 11 in case of noisy data.

In Figure 12, the detected objects with $\lambda = 10^{-3}$, for p $\in \{0, 0.1\%, 1\%\}$ noisy data (58), after 3500 iterations, are visualized. The Trefftz method with regularized least–squares minimization (57) shows a good performance in detecting the circle for small noisy data. However, the reconstruction becomes more sensitive and deteriorates as the amount of noise increases, indicating the limitations of the information content that the noisy measured data (58) encapsulates.

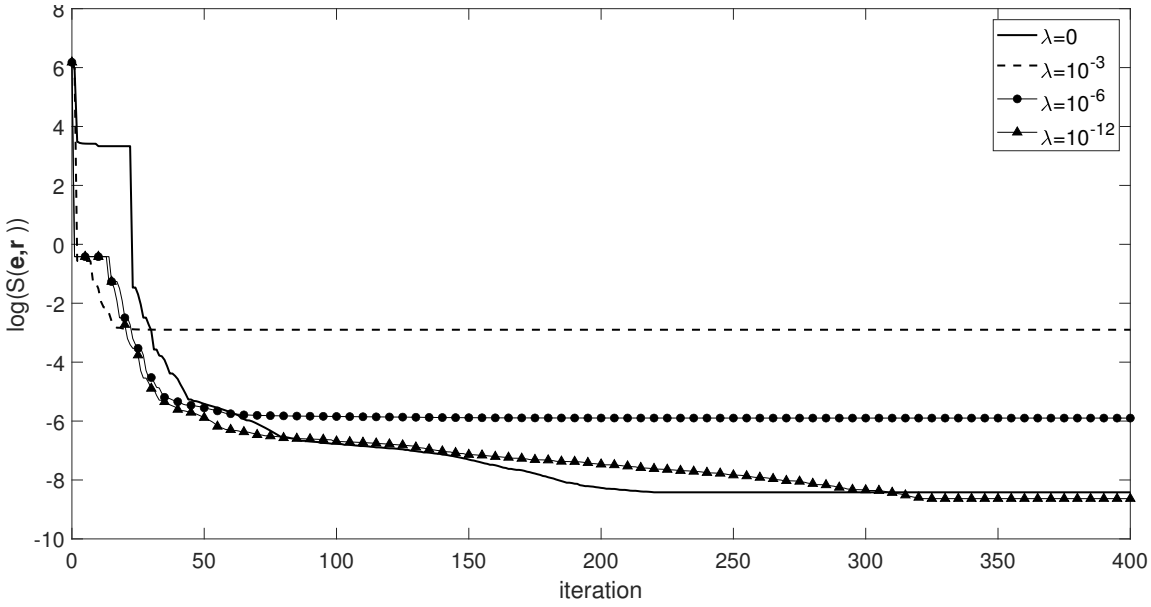

Figure 8: The objective function (57) versus the number of iterations for $\lambda \in \{0, 10^{-12}, 10^{-6}, 10^{-3}\}$ when the data (58) is noiseless, i.e. p = 0. The CPU times required for these computations were 367 seconds, 362 seconds, 361 seconds and 359 seconds for $\lambda = 0$, $\lambda = 10^{-12}$, $\lambda = 10^{-6}$ and $\lambda = 10^{-3}$, respectively.

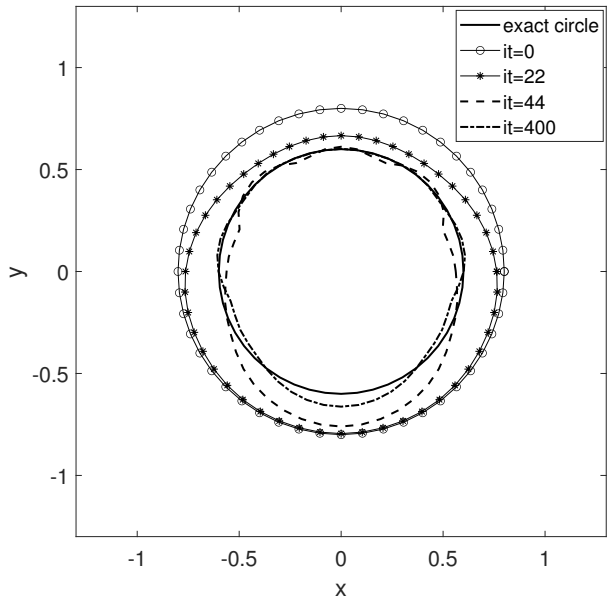

Figure 9: The detected object at various iterations, without regularization ($\lambda = 0$), when the data (58) is noiseless.

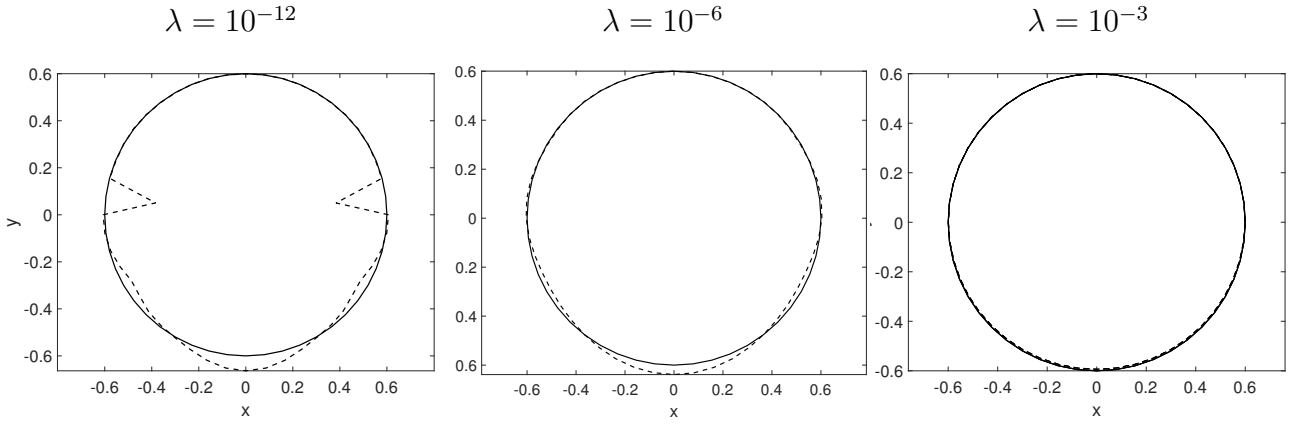

Figure 10: The detected object after 400 iterations for various regularization parameters λ. The dotted lines are the inverse problem solutions and the continuous lines show the exact circular boundary of the immersed object.

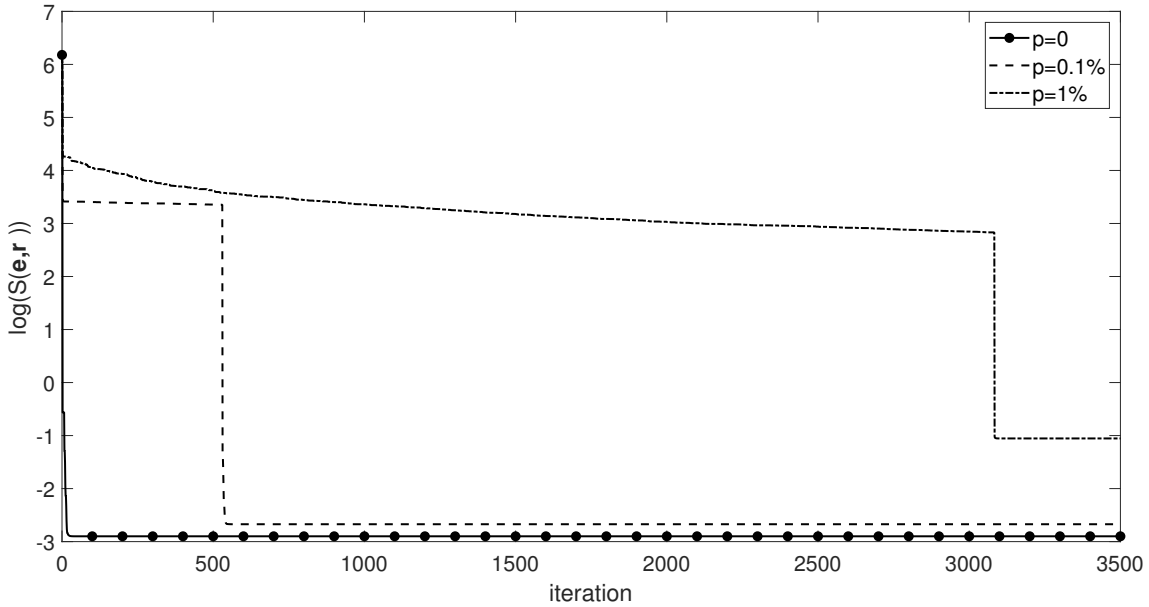

Figure 11: The objective function (57) versus the number of iterations for $\lambda = 10^{-3}$, when the data (58) is contaminated by $\mathrm{p} \in \{0, 0.1\%, 1\%\}$ noise. The CPU times expended for these computations were 3254 seconds, 3099 seconds and 3131 seconds for $p = 0$, $p = 0.1\%$ and $p = 1\%$, respectively.

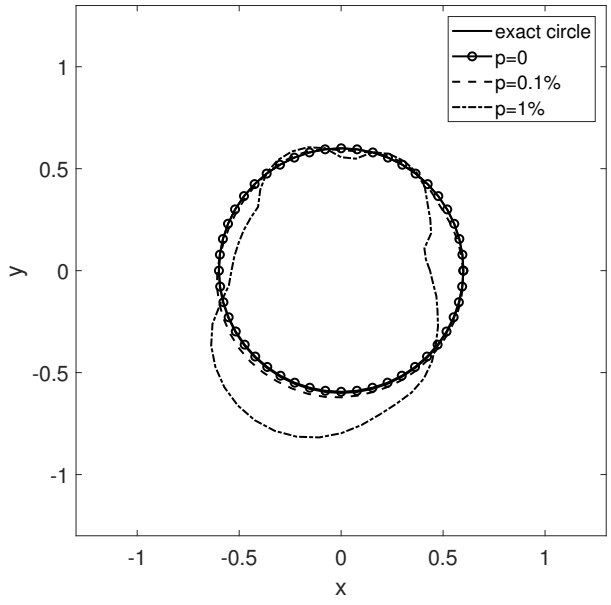

Figure 12: The detected objects with $\lambda = 10^{-3}$, for $\mathrm{p} \in \{0, 0.1\%, 1\%\}$ noisy data (58), after 3500 iterations.

6.1 Detection of a pear–shaped domain

In this example, we consider a more complicated pear–shaped domain D with its boundary Γ given by the radial representation [35],

$$r(\theta) = \frac{1}{3.5}\sqrt{(-0.25 + 1.3\cos(\theta) + 0.5\cos(2\theta))^2 + 2.25\sin^2(\theta)}, \quad \theta \in [0, 2\pi). \tag{60}$$

In this case the inward normal derivative to Γ is given by

$$\mathbf{n}(\theta) = \frac{1}{\sqrt{r^2(\theta) + (r')^2(\theta)}}\Big(-r'(\theta)\sin(\theta) - r(\theta)\cos(\theta), r'(\theta)\cos(\theta) - r(\theta)\sin(\theta)\Big).$$

We take the Dirichlet data (3) to be

$$f_1(x) = \mathrm{e}^{-x^2}, \quad f_2(x) = 0, \quad x \in \mathbb{R}, \tag{61}$$

on the upper boundary ($y = h = 1$). Since in this case no analytical solution is available, the vorticity $f_3(x) = \Delta\psi(x, 1)$ and its slope $f_4(x) = \dfrac{\partial(\Delta\psi)}{\partial y}(x, 1)$ for $x \in \mathbb{R}$, are numerically simulated by solving, using the Trefftz method, the direct well–posed problem

$$\begin{cases} \Delta^2\psi = 0, & \text{in } \Omega \setminus \overline{D}, \\ \psi(x, 1) = \mathrm{e}^{-x^2}, & x \in \mathbb{R}, \\ \dfrac{\partial\psi}{\partial y}(x, 1) = 0, & x \in \mathbb{R}, \\ \psi = 0, & \text{on} \quad \Gamma, \\ \dfrac{\partial\psi}{\partial n} = 0, & \text{on} \quad \Gamma, \end{cases} \tag{62}$$

where $\dfrac{\partial\psi}{\partial n}$ is the normal derivative of ψ on Γ. For the well-posedness of the direct problem (62), see [3]. Since the data in (61) decays rapidly at $\pm\infty$, we take $L = 3$ in (27) and (28).

Figures 13–15 display the numerical results of the direct problem (62) when $N = 187$, $M = 150$ and $\mathrm{N} = 14$.

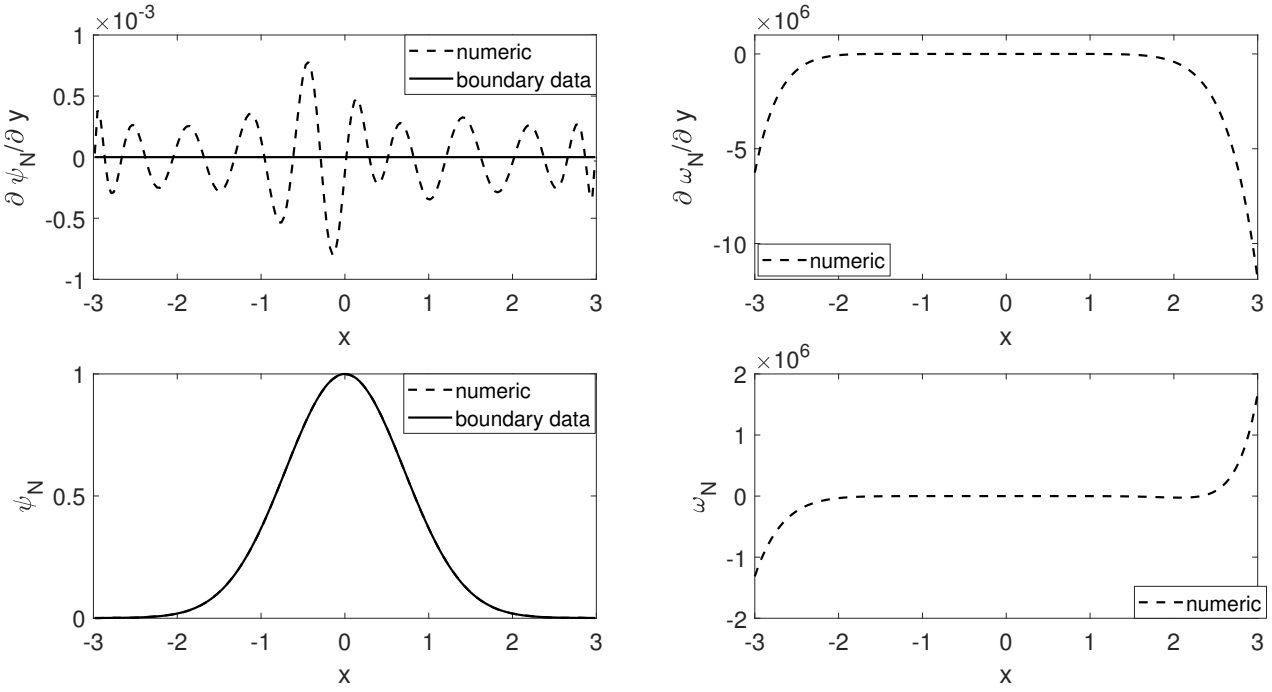

Figure 13: Trefftz method approximations of the direct problem (62) on the upper boundary $y = h = 1$, as functions of $x \in (-L, L) = (-3, 3)$, obtained with $N = 187$, $M = 150$ and $\mathrm{N} = 14$, in comparison with the available boundary data (61).

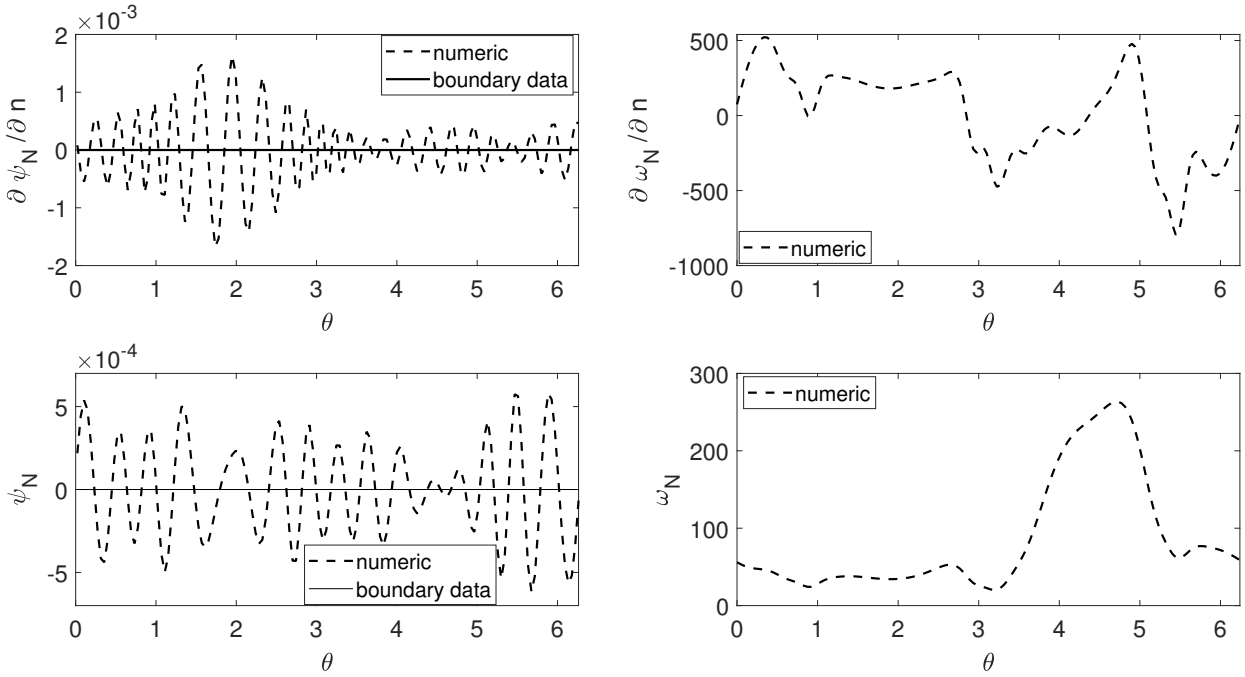

Figure 14: Trefftz method approximations of the direct problem (62) on the inner boundary $r = r(\theta)$ given by eq. (60), as functions of $\theta \in [0, 2\pi)$, obtained with $N = 187$, $M = 150$ and $\mathrm{N} = 14$, in comparison with the available boundary data $\psi = \partial\psi/\partial n = 0$, see (62).

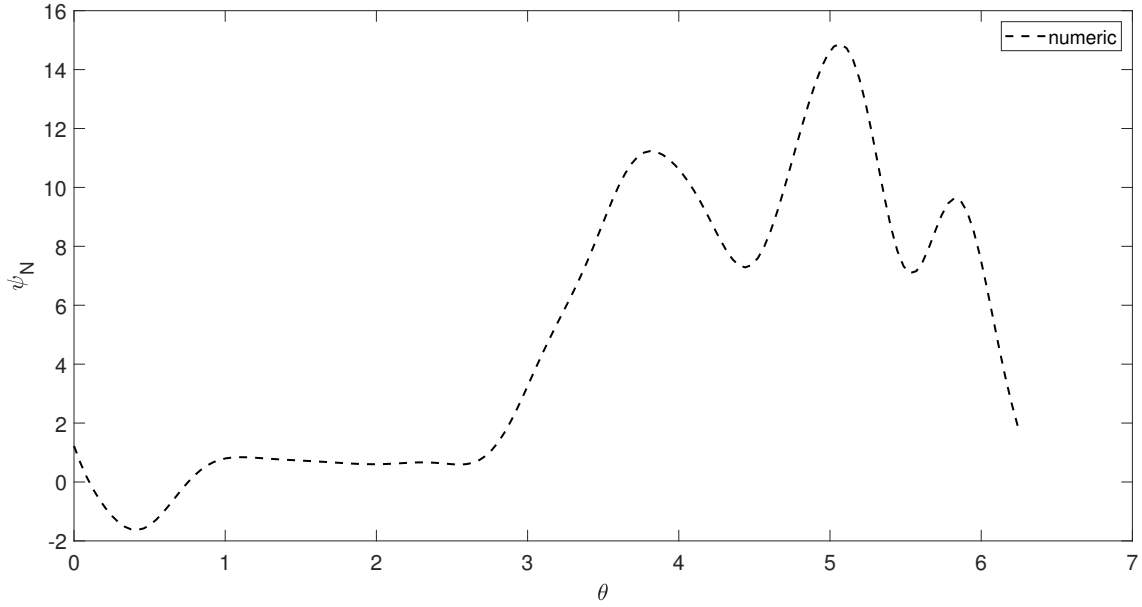

Figure 15: Trefftz method approximation of the direct problem (62) on the interior circle $r = 0.8$, as a function of $\theta \in [0, 2\pi)$, obtained with $N = 187$, $M = 150$ and $\mathrm{N} = 14$.

From Figures 13 and 14 it can be observed that there is a very good agreement between the numerical solutions and the exact input data for ψ and $\partial\psi/\partial n$ on the boundary

$$\{(x, h = 1) \,|\, x \in (-L, L) = (-3, 3)\} \cup \{r(\theta)(\cos(\theta), \sin(\theta)) \,|\, \theta \in [0, 2\pi)\}\,.$$

The numerically obtained data for $f_3(x) = \omega_{\rm N}(x)$ and $f_4(x) = (\partial\omega_{\rm N}/\partial n)(x)$ for $x \in (-L, L) = (-3, 3)$ shown in Figure 13 was used as input in the minimization of (57), but the results were not satisfactory manifesting high instabilities. In order to overcome this difficulty, we employ a model reduction by replacing the general representation (55) with a finite parametrization using trigonometric polynomials given by

$$r(\theta) = a_0 + \sum_{k=1}^{K} \left(a_k \cos(k\theta) + b_k \sin(k\theta)\right), \quad \theta \in [0, 2\pi), \tag{63}$$

where the vectors of unknown coefficients $\mathbf{a} = (a_k)_{k=\overline{0,K}}$ and $\mathbf{b} = (b_k)_{k=\overline{1,K}}$ are replacing the vector $\mathbf{r} = (r_k)_{k=\overline{1,M}}$ in (57). We also need to replace the constraints (59) by $-\mathbf{0.7} < \mathbf{a}, \mathbf{b} < \mathbf{0.7}$. The initial guesses for $\mathbf{a}$ and $\mathbf{b}$ are randomly selected within a $\pm 20\%$ perturbation of the simulated values for $\mathbf{a}$ and $\mathbf{b}$ obtained by fitting (in a least–squares sense) the approximation (63) with $K = 6$, the exact pear–shaped image radial function (60). As can be seen from Figure 13, the f_3 and f_4 data, generated by solving the direct problem (62), are large near the end points of $(-3, 3)$ which leads to convergence issues in the solution of the inverse problem. To overcome this difficulty, we solve the direct problem for $L = 3$, but collect the f_3 and f_4 data from the interval $(-2, 2)$ and then solve the inverse problem when $L = 2$. The upper boundary discretization is adjusted accordingly by taking $N = 125$ while keeping M and N the same as in the direct problem to $M = 150$ and $\mathrm{N} = 14$. Noise is added to the boundary data f_3 and f_4 by taking

$$f_\ell^{(\mathrm{p})}(\mathbf{x}^i) = (1 + \rho_i\, \mathrm{p})\, f_\ell(\mathbf{x}^i), \quad i = \overline{1, N}, \quad \ell = 3, 4, \tag{64}$$

the objective function

$$\begin{aligned} S(\mathbf{e}, \mathbf{a}, \mathbf{b}) := \sum_{i=1}^{N} \Big[&\left\{\psi_{\rm N}(\mathbf{e}, \mathbf{x}^i) - f_1(\mathbf{x}^i)\right\}^2 + \left\{\frac{\partial \psi_{\rm N}}{\partial y}(\mathbf{e}, \mathbf{x}^i) - f_2(\mathbf{x}^i)\right\}^2 \\ &+ \left\{\Delta\psi_{\rm N}(\mathbf{e}, \mathbf{x}^i) - f_3^{(\mathrm{p})}(\mathbf{x}^i)\right\}^2 + \left\{\frac{\partial(\Delta\psi_{\rm N})}{\partial y}(\mathbf{e}, \mathbf{x}^i) - f_4^{(\mathrm{p})}(\mathbf{x}^i)\right\}^2 \Big] \\ &+ \sum_{k=N+1}^{N+M} \left[\psi_{\rm N}(\mathbf{e}, \mathbf{x}^k)\right]^2 + \lambda_1 \sum_{i=1}^{8\mathrm{N}+4} e_i^2 + \lambda_2 \left[\sum_{k=0}^{K} a_i^2 + \sum_{k=1}^{K} b_i^2\right], \end{aligned} \tag{65}$$

is minimized. Since the inverse geometric obstacle problem under investigation is ill-posed we have found necessary to stop the iterations at appropriate thresholds before the instabilities start to manifest. The numerically obtained results illustrated in Figures 16 and 17 show accurate and stable reconstructions of the pear-shaped domain (60).

As a second investigation for this example we solve the inverse problem on $(-3, 3)$ (i.e. $L = 3$), but only use f_3 and f_4 data from $(-2, 2)$ to overcome the difficulties due to the large values in f_3 and f_4 close to end points of the interval $(-3, 3)$ and also to consider the case of partial measurements of f_3 and f_4. In the objective function given by (65), we still take $N = 187$, $M = 150$ and $\mathrm{N} = 14$, but in the third and the fourth terms we only use the nodes $\mathbf{x}^i \in (-2, 2)$ and ignore the rest. The convergence of the objective function and the reconstructed objects are depicted in Figures 18 and 19, respectively. When there is no noise in the f_3 and f_4 data, regularization with $\lambda_1 = 0$, $\lambda_2 = 0.1$ performs well in the detection of the obstacle. That is, no regularization is required for the coefficients $\mathbf{e}$ of the Trefftz approximation. However, when $\mathrm{p} = 0.1\%$ noise is added, both $\mathbf{e}$ and $(\mathbf{a}, \mathbf{b})$ need to be regularized by taking $\lambda_1 = \lambda_2 = 0.1$ in (65).

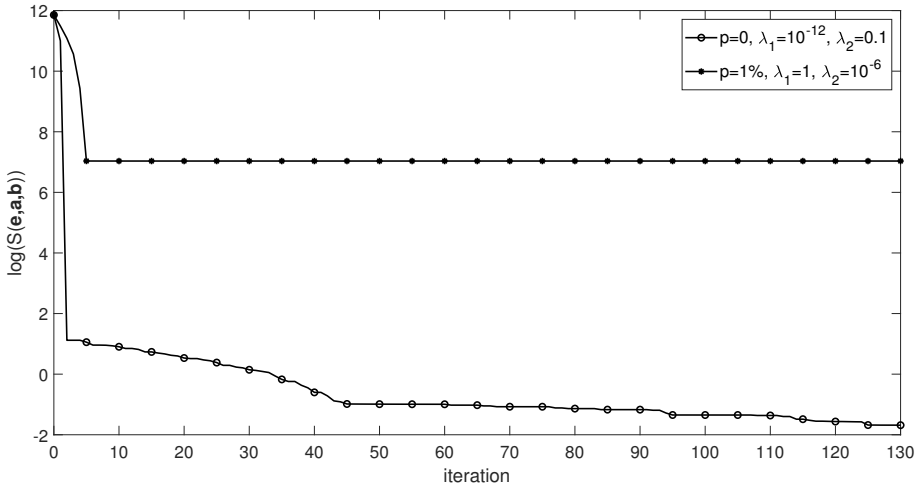

Figure 16: Convergence of the objective function $S(\mathbf{e}, \mathbf{a}, \mathbf{b})$ given by (65) when there is p $\in \{0, 1\%\}$ noise in the data f_3 and f_4, with the corresponding regularization parameters. The CPU times expended for these computations were 301 seconds and 314 seconds for $p = 0$ and $p = 1\%$, respectively.

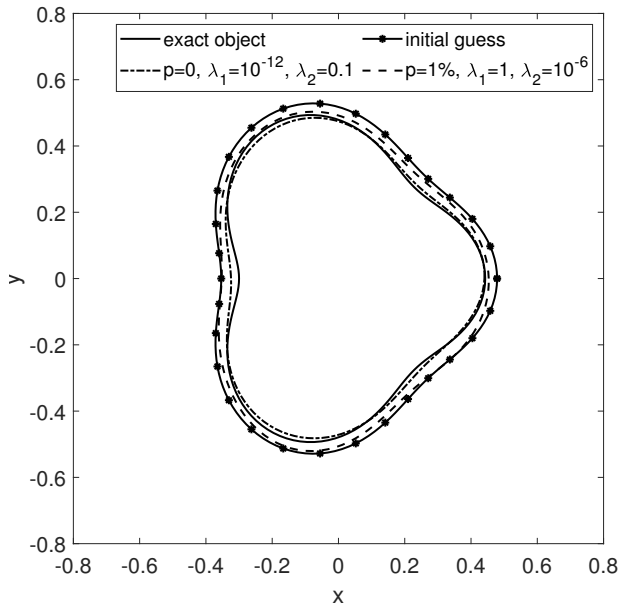

Figure 17: The exact object, the initial guess in the `lsqnonlin` routine and the reconstructed obstacles in case of the finite-dimensional parametrization (63) with $K = 6$ for p $\in \{0, 1\%\}$ noise in the f_3 and f_4 data, and corresponding regularization parameters.

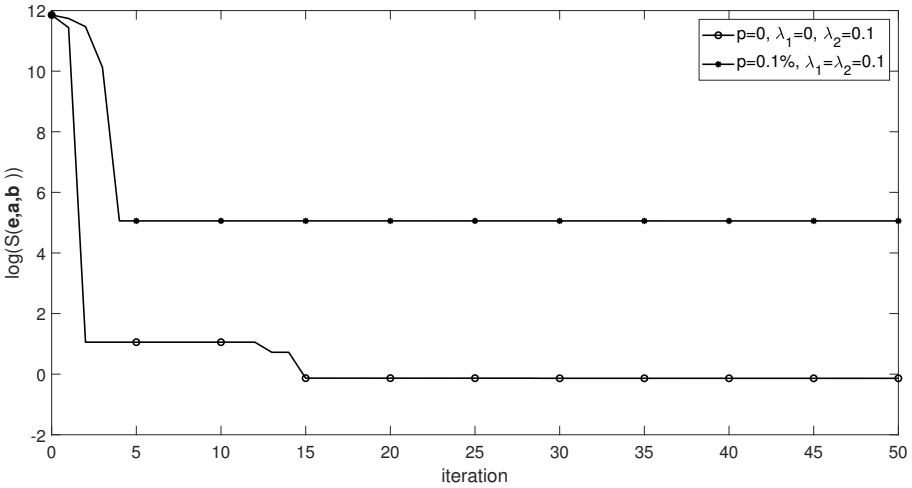

Figure 18: Convergence of the objective function $S(\mathbf{e}, \mathbf{a}, \mathbf{b})$ given by (65) when $L = 3$ and the data f_3 and f_4 are taken from $(-2, 2)$ for p $\in \{0, 0.1\%\}$ noise, with the corresponding regularization parameters. The required CPU times for these computations were 154 seconds and 155 seconds for $p = 0$ and $p = 0.1\%$, respectively.

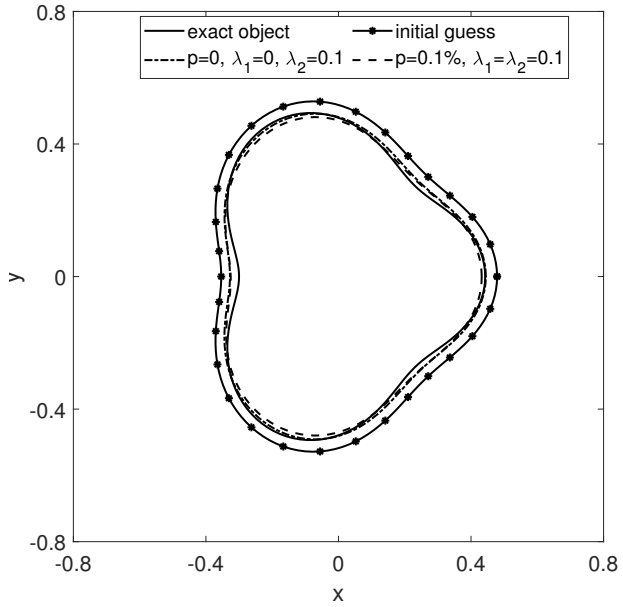

Figure 19: The exact object, the initial guess in the `lsqnonlin` routine and the reconstructed obstacles in case of the finite-dimensional parametrization (63) with $K = 6$ when $L = 3$ and f_3 and f_4 data are taken from $(-2, 2)$ for p $\in \{0, 0.1\%\}$ with the corresponding regularization parameters.

7 Conclusions

We have applied, apparently for the first time, the MFS and the Trefftz method for the numerical solution of direct boundary value problems for the two–dimensional biharmonic equation in a special unbounded domain exterior of an obstacle but bounded above by a horizontal fluid level $y = h$. Both methods, when applied to the direct problem produced highly accurate results. For the associated inverse geometric problem, the MFS failed to yield satisfactorily accurate reconstructions. Contrarily, the Trefftz method, applied iteratively for minimizing the

nonlinear Tikhonov regularising functional subject to simple bounds on the variables, yielded accurate and stable reconstructions of the unknown submerged obstacle. Several challenges were encountered in this application (e.g., for the irregular pear-shaped example (60), a model reduction based on trigonometric polynomials parametrisation (63) was required), but the numerical results presented and discussed for two different examples indicate that accurate and stable reconstructions of the obstacle from (up to 1%) noisy measurements of the unspecified values on the top horizontal boundary can be reproduced with the proposed method. Other examples involving the retrieval of different obstacle shapes such as a peanut, bean or kite [22, 29, 35] are likely to present similar features and challenges to those encountered for the pear–shape (60) investigated in Section 6.1. Possible areas of future extensions are: (i) the detection of multiple obstacles and (ii) unsteady Stokes flows with an unknown obstacle [40].

Acknowledgements

This study was supported by the Scientific and Technological Research Council of Türkiye (TUBITAK) [Pelin Senel, Grant Number: 1059B192400304].

References

[1] C. Alvarez, C. Conca, L. Friz, O. Kavian and J.H. Ortega. Identification of immersed obstacles via boundary measurements, *Inverse Problems*, **21**:1531–1552, 2005.

[2] C. Alvarez, C. Conca, R. Lecaros and J.H. Ortega. On the identification of a rigid body immersed in a fluid: A numerical approach, *Engineering Analysis with Boundary Elements*, **32**:919–925, 2008.

[3] C. Amrouche and M. Fontes. Biharmonic problem in exterior domains, *Comptes Rendus Mathematique*, **338**:121–126, 2004.

[4] A. Bogomolny. Fundamental solutions method for elliptic boundary value problems, *SIAM Journal on Numerical Analysis*, **22**:644–669, 1985.

[5] C.S. Chen, H.A. Cho and M.A. Golberg. Some comments on the ill-conditioning of the method of fundamental solutions, *Engineering Analysis with Boundary Elements*, **30**: 405-410, 2006.

[6] J.-T. Chen, Y.-T. Lee, S.-R. Yu and S.-C. Shieh. Equivalence between the Trefftz method and the method of fundamental solutions for the annular Green's function using the addition theorem and the image concept, *Engineering Analysis with Boundary Elements*, **33**:678–688, 2009.

[7] J.-T. Chen, C.S. Wu, Y.-T. Lee and K.H. Chen. On the equivalence of the Trefftz method and method of fundamental solutions for Laplace and biharmonic equations, *Computers and Mathematics with Applications*, **53**:851–879, 2007.

[8] A.H.D. Cheng, C.S. Chen and A. Karageorghis. *An Introduction to the Method of Fundamental Solutions*, World Scientific, Singapore, 2025.

[9] D. Colton and R. Kress. *Inverse Acoustic and Electromagnetic Scattering Theory*, Springer, Berlin, 4th edition, 2019.

[10] B.H. Dennis, G.S. Dulikravich and S. Yoshimura. A finite element formulation for the determination of unknown boundary conditions for three-dimensional steady thermoelastic problems, *Journal of Heat Transfer*, **126**:110–118, 2004.

[11] T. El-Bashir. *Fluid Flow at Small Reynolds Number: Numerical Applications*, Hikari Ltd., Oman, 2006.

[12] H.W. Engl, M. Hanke and A. Neubauer. *Regularization of Inverse Problems*, Springer, Berlin, 1996.

[13] C.-M. Fan and H.-F. Chan. Modified collocation Trefftz method for the geometry boundary identification problem of heat conduction, *Numerical Heat Transfer, Part B*, **59**: 58-75, 2011.

[14] B. Fuglede. On a direct method of integral equations for solving the biharmonic Dirichlet problem, *ZAMM*, **61**:449–459, 1981.

[15] C. Gáspár and A. Karageorghis. Method of fundamental solutions formulations for biharmonic problems, *Engineering Analysis with Boundary Elements*, **175**, Article iD. 106180, 2025.

[16] H. Gourgeon and I. Herrera. Boundary methods. c-complete systems for the biharmonic equations, In: *Boundary Element Methods*, (ed. C.A. Brebbia), Springer-Verlag, Berlin, pp.431-441, 1981.

[17] P.C. Hansen. Analysis of discrete ill-posed problems by means of the L-curve, *SIAM Review*, **34**:561–580, 1992.

[18] U. Heise. Numerical properties of integral equations in which the given boundary values and the sought solution are defined on different curves, *Computers and Structures*, **8**:199–205, 1978.

[19] I. Herrera. Trefftz method. In: *Topics in Boundary Element Research*, (ed. C.A. Brebbia), Springer-Verlag, Berlin, pp.225-253, 1984.

[20] V. Isakov. Inverse obstacle problems, *Inverse Problems*, **25**, Article ID. 123002, 2009.

[21] V. Isakov. *Inverse Problems for Partial Differential Equations*, Springer, Berlin, 3rd edition, 2017.

[22] O. Ivanysyn and R. Kress. Nonlinear integral equations for solving inverse boundary value problems for inclusions and cracks, *Journal of Integral Equations and Applications*, **18**:13–38, 2006.

[23] W.G. Jin, Y.K. Cheung and O.C. Zienkiewicz. Application of the Trefftz method in plane elasticity problems, *International Journal for Numerical Methods in Engineering*, **30**:1147–1161, 1990.

[24] W.G. Jin, Y.K. Cheung and O.C. Zienkiewicz. Trefftz method for Kirchhoff plate bending problems, *International Journal for Numerical Methods in Engineering*, **36**:765–781, 1993.

[25] A. Karageorghis and G. Fairweather. The method of fundamental solutions for the numerical solution of the biharmonic equation, *Journal of Computational Physics*, **69**:434–459, 1987.

[26] A. Karageorghis and G. Fairweather. The Almansi method of fundamental solutions for solving biharmonic problems, *International Journal for Numerical Methods in Engineering*, **26**:1665–1682, 1988.

[27] A. Karageorghis and G. Fairweather. The simple layer potential method of fundamental solutions for certain biharmonic problems, *International Journal for Numerical Methods in Fluids*, **9**:1221–1234, 1989.

[28] A. Karageorghis, D. Lesnic and L. Marin. A moving pseudo-boundary MFS for void detection, *Numerical Methods for Partial Differential Equations*, **29**: 935-960, 2013.

[29] A. Karageorghis, D. Lesnic and L. Marin. Regularized collocation Trefftz method for void detection in two-dimensional steady-state heat conduction problems, *Inverse Problems in Science and Engineering*, **22**: 395-418, 2014.

[30] J.A. Kolodziej and A.P. Zielinski. *Boundary Collocation Techniques and their Application in Engineering*, WIT Presss, Southampton, 2009.

[31] R. Kress, A. Mohsen and B. Brosowski. On the simulation source technique for exterior problems in acoustics, *Mathematical Methods in the Applied Sciences*, **8**:585–597, 1986.

[32] D. Kupradze and M.A. Aleksizde. The method of functional equations for an approximate solution of certain boundary value problems, *USSR Computational Mathematics and Mathematical Physics*, **4**:82–126, 1964.

[33] Z.-C. Li, M.-G Lee, Z.Y.Chiang and Y.P. Liu. The Trefftz method using fundamental solutions for biharmonic equations, *Journal of Computational and Applied Mathematics*, **235**:4350-4367, 2011.

[34] L. Marin and D. Lesnic. The method of fundamental solutions for inverse boundary value problems associated with the two dimensional biharmonic equation, *Mathematical and Computer Modelling*, **42**:261–278, 2005.

[35] N.F.M. Martins and A.L. Silvestre. An iterative MFS approach for the detection of immersed obstacles, *Engineering Analysis with Boundary Elements*, **32**:517–524, 2008.

[36] D. de Mey. Integral equations for potential problems with the source function not located on the boundary, *Computers and Structures*, **8**:113–115, 1978.

[37] A.G. Ramm. An inverse problem for biharmonic equation, *International Journal of Mathematics and Mathematical Sciences*, **11**:413–415, 1988.

[38] T. Shigeta and D.L. Young. Mathematical and numerical studies on meshless methods for exterior unbounded domain problems, *Journal of Computational Physics*, **230**:6900–6915, 2011.

[39] A.N. Tikhonov, A.S. Leonov and A.G. Yagola. *Nonlinear Ill-posed Problems*, Chapman & Hall, London, 1998.

[40] W. Yan, Y. He and Y. Ma. Shape inverse problem for the two-dimensional unsteady Stokes flow, *Numerical Methods for Partial Differential Equations*, **26**:690-701, 2010.

[41] A. Zeb, D.B. Ingham and D. Lesnic. The method of fundamental solutions for a biharmonic inverse boundary determination problem, *Computational Mechanics*, **42**:371–379, 2008.